



Unique ocean circulation pathways reshape the Indian Ocean oxygen minimum zone with warming

Sam Ditkovsky¹, Laure Resplandy², and Julius Busecke³

¹Program in Atmospheric and Oceanic Sciences, Princeton University, Princeton, NJ, USA

²Department of Geosciences and High Meadows Environmental Institute, Princeton University, Princeton, NJ, USA

³Lamont-Doherty Earth Observatory, Columbia University, New York, NY, USA

Correspondence: Sam Ditkovsky (samjd@princeton.edu) and Laure Resplandy (laurer@princeton.edu)

Received: 22 May 2023 – Discussion started: 25 May 2023

Revised: 13 September 2023 – Accepted: 9 October 2023 – Published: 29 November 2023

Abstract. The global ocean is losing oxygen with warming. Observations and Earth system model projections, however, suggest that this global ocean deoxygenation does not equate to a simple and systematic expansion of tropical oxygen minimum zones (OMZs). Previous studies have focused on the Pacific Ocean; they showed that the outer OMZ deoxygenates and expands as oxygen supply by advective transport weakens, the OMZ core oxygenates and contracts due to a shift in the composition of the source waters supplied by slow mixing, and in between these two regimes oxygen is redistributed with little effect on OMZ volume. Here, we examine the OMZ response to warming in the Indian Ocean using an ensemble of Earth system model high-emissions scenario experiments from the Coupled Model Intercomparison Project Phase 6. We find a similar expansion–redistribution–contraction response but show that the unique ocean circulation pathways of the Indian Ocean lead to far more prominent OMZ contraction and redistribution regimes than in the Pacific Ocean. As a result, only the outermost volumes (oxygen $> 180 \mu\text{mol kg}^{-1}$) expand. The Indian Ocean experiences a broad oxygenation in the southwest driven by a reduction in waters supplied by the Indonesian Throughflow in favor of high-oxygen waters supplied from the southern Indian Ocean gyre. Models also project a strong localized deoxygenation in the northern Arabian Sea due to the rapid warming and shoaling of marginal sea outflows (Red Sea and Persian Gulf) and increases in local stratification with warming. We extend the existing conceptual framework used to explain the Pacific OMZ response to interpret the response in the Indian Ocean.

1 Introduction

Oxygen minimum zones (OMZs) are naturally occurring low-oxygen regions located in subsurface tropical oceans (typically 100–1500 m). OMZs develop in the “shadow zones” of the ocean thermocline, where oxygen supply by ocean circulation is weak (Luyten et al., 1983; Pedlosky, 1983), and are generally located below highly productive surface systems that boost respiration and biological oxygen demand at the subsurface (Paulmier and Ruiz-Pino, 2009). The global ocean has lost oxygen in response to global warming (Keeling et al., 2010; Helm et al., 2011; Schmidtko et al., 2017; Bindoff et al., 2019), and this trend is expected to continue and accelerate over the twenty-first century if anthropogenic emissions are not significantly drawn down (Bopp et al., 2013; Kwiatkowski et al., 2020). Global deoxygenation has been attributed to weakening ocean ventilation (i.e., weakening oxygen supply by ocean circulation and mixing) and decreasing oxygen solubility in seawater with warming (e.g., Oschlies et al., 2018). A concern is that OMZs are expanding in response to global deoxygenation, potentially disrupting the physiology and survival of marine organisms and compressing the habitats of marine species requiring oxygen for their survival (Vaquer-Sunyer and Duarte, 2008; Miller et al., 2002; Stramma et al., 2008, 2012; Deutsch et al., 2020; Levin, 2018). The fate of OMZs under warming, in particular the two most intense regions found in the tropical Pacific Ocean and tropical Indian Ocean, however, has been highly debated, with apparently inconsistent changes found across hydrographic observations, paleo-oceanographic proxies, and Earth sys-

tem model (ESM) projections. In situ hydrographic observations collected since the 1950s suggest that the tropical Indo-Pacific oceans and the marginal seas that supply oxygen to the tropical Indian Ocean (including the Persian Gulf and Red Sea) have lost oxygen, supporting the view that tropical OMZs are expanding (Stramma et al., 2008; Helm et al., 2011; Ito et al., 2017; Banse et al., 2014; Piontkovski and Al-Oufi, 2015; Queste et al., 2018; Naqvi, 2021). Yet, paleo-oceanographic studies suggest that the OMZ in the eastern tropical Pacific Ocean has contracted, rather than expanded, under past warming conditions (Deutsch et al., 2014; Auderset et al., 2022). Looking into the future, studies using ESM ensembles have projected a robust deoxygenation at middle and high latitudes with warming, consistent with the weakening of ventilation found at the global scale, but have failed, until recently, to reach a consensus on the expected changes in oxygen and OMZ volumes in tropical oceans (Cocco et al., 2013; Bopp et al., 2013, 2017; Cabré et al., 2015; Resplandy, 2018; Kwiatkowski et al., 2020).

Busecke et al. (2022) recently showed that the inconsistencies found in the fate of the OMZ in the Pacific Ocean could be reconciled using an ensemble of ESMs from the Coupled Model Intercomparison Project Phase 6 (CMIP6; Eyring et al., 2016). They found that the OMZ response to global warming was in fact consistent across the ESMs when examined in an oxygen-space framework and fell into three regimes: an expansion of the OMZ outer layers (large OMZ volume delimited by oxygen thresholds of typically $\sim 100 \mu\text{mol kg}^{-1}$ or higher), a contraction of the eastern Pacific “OMZ core” waters (OMZ volume delimited by oxygen thresholds of $\sim 20 \mu\text{mol kg}^{-1}$ or lower), and a “transition regime” between contraction and expansion that experiences weak and uncertain changes associated with a spatial redistribution of the OMZ volume. This three-regime framework reconciles hydrographic work that shows an OMZ expansion in the central Pacific Ocean where the OMZ outer layers are located (Stramma et al., 2008) and paleo-oceanographic studies that found evidence of a contraction in the eastern Pacific (note that these studies used nitrogen isotopes which are a proxy for OMZ core denitrifying waters; Deutsch et al., 2014; Auderset et al., 2022). The framework also explains the discrepancies found in previous modeling studies that often considered OMZ volume definitions that fall in the transition regime where changes are smaller and uncertain (e.g., Bopp et al., 2013; Cabré et al., 2015). In the Pacific Ocean, the apparent discrepancy between outer OMZ expansion and core contraction can be interpreted using the conceptual framework proposed by Gnanadesikan et al. (2007), which distinguishes between two models of ocean ventilation: (1) a “single-pipe” model where ventilation is controlled by advection from one source water mass and (2) a “mixing network” model in which ventilation rates are sustained by slow mixing of multiple source waters as in ocean shadow zones (Lévy et al., 2022; Gnanadesikan et al., 2013; Brandt et al., 2015). As ocean circulation pathways weaken,

regions ventilated by a single pipe experience reduced supply of oxygen (transport rates of oxygenated surface water to the thermocline slow), while regions ventilated by a mixing network can either experience a reduction or increase in ventilation and oxygen supply (by changing the connectivity and the contributions of each source water to the mixing network). The single-pipe model explains the deoxygenation of the outer OMZ layers, which has been attributed to the weakening of the northern and southern subtropical cells that ventilate the outer layers of the OMZ (Gnanadesikan et al., 2012; Duteil et al., 2014, 2021; Busecke et al., 2022; Llanillo et al., 2018; Margolskee et al., 2019). In contrast, changes in mixing network connectivity explain the oxygenation of the Pacific OMZ core, which was attributed to reduced contributions from aged, oxygen-poor deep and intermediate waters, shifting the mixing ratio towards younger, oxygen-rich, upper-ocean waters (Bryan et al., 2006; Gnanadesikan et al., 2007, 2012; Takano et al., 2018; Busecke et al., 2022).

The fate of the Indian Ocean OMZ has been far less studied than its Pacific Ocean counterpart. Yet, the Indian Ocean shows some of the fastest ocean warming trends in the world (Roxy et al., 2014; Sharma et al., 2023), and the expansion of its OMZ could have detrimental effects for coastal populations that depend heavily on marine resources for food security and economic stability in the region (Bouchard and Crumplin, 2010; Clifton et al., 2012; Gattuso et al., 2015; Llewellyn et al., 2016; Roy, 2019). The ventilation pathways and OMZ geometry in the Indian Ocean are fundamentally different from the two subtropical cells (one in each hemisphere) and eastern-boundary OMZ found in the Pacific Ocean. It is thus unclear whether the single-pipe and mixing network framework which characterizes the Pacific Ocean is sufficient to describe the behavior of the Indian Ocean. The Indian Ocean is bounded by continent to the north and ventilation is almost exclusively sustained by one subtropical cell originating in the southern Indian Ocean gyre (Harper, 2000; Schott et al., 2002; Phillips et al., 2021). As a result, oxygen levels are higher in the southern Indian Ocean, while an OMZ extends over most of the Arabian Sea and the Bay of Bengal in the north (see Fig. 1 for observed climatological oxygen field and major ventilation pathways). Other peculiarities of the Indian Ocean ventilation are the Indonesian Throughflow, which brings waters from the tropical Pacific Ocean into the southern Indian Ocean (Sprintall et al., 2009), and the saline marginal sea outflow waters from the Red Sea and Persian Gulf that ventilate the Arabian Sea (Rhein et al., 1997; Beal et al., 2000; Menezes, 2021; Sheehan et al., 2020). Ventilation by all these advective pathways (southern gyre, Indonesian Throughflow, and marginal seas) is projected to weaken in response to climate change (Sen Gupta et al., 2016; Feng et al., 2017; Stellema et al., 2019; Lachkar et al., 2019; Kobayashi et al., 2012), but the extent to which these changes in ventilation will affect basin-scale oxygen content and the OMZ in the Indian Ocean, however, is still poorly constrained. Here, we examine changes in oxygen

content and OMZ volume in the Indian Ocean in response to climate change using an ensemble of CMIP6-generation ESMs with a focus on thermocline depths (upper 1000 m). We show that the fate of the Indian Ocean OMZ is consistent with the three-regime framework identified in the Pacific Ocean (Busecke et al., 2022) but that broad oxygenation results in a much more prominent contraction regime in the Indian Ocean than in the Pacific Ocean. Interpreting these changes in oxygen and OMZ volume in the Indian Ocean calls for an extension of the single-pipe and mixing network conceptual framework to include the unique contributions from the Indonesian Throughflow and marginal seas, which we show can be interpreted as “two-pipe” and “moving-pipe” systems.

2 Methods

2.1 Datasets

We use an ensemble of eight ESMs from the CMIP6 archive (Eyring et al., 2016; O’Neill et al., 2016). Out of the 14 CMIP6 ESMs that provided monthly dissolved oxygen data for the pre-industrial control, historical, and SSP5-8.5 experiments (Busecke et al., 2022), we exclude six models that simulate virtually no suboxic ($\leq 10 \mu\text{mol kg}^{-1}$) volume in the Arabian Sea (ACCESS-ESM1-5, CanESM5, CanESM5-CanOE, CNRM-ESM2-1, IPSL-CM6A-LR; Table S1 in the Supplement). We keep the eight remaining ESMs (GFDL-CM4, GFDL-ESM4, MIROC-ES2L, MPI-ESM1-2-HR, MPI-ESM1-2-LR, NorESM2-LM, NorESM2-MM, UKESM1-0-LL). All six ESMs excluded from the multi-model mean exhibit above-average salinity biases in the Arabian Sea, likely from outflows (Fig. S1 in the Supplement), and four of six models exhibit Red Sea outflow rates over twice the observed rate (Fig. S2). Thus, the representation of marginal sea outflows may be improved significantly in our ensemble by excluding these ESMs. For this analysis, we use oxygen, salinity, and potential temperature for all eight models. When available, we also use output for ideal age (available for six ESMs), export of organic carbon at 100 m (available for seven ESMs), and mass transport (available for five ESMs). Stratification is calculated from potential temperature and salinity fields using the GSW Python package (Firing et al., 2021). To limit computational costs of this study and because we expect inter-model variability in dissolved oxygen to dominate over internal variability, only one member is used for each model. See Table 1 for member labels and data availability of each model. All model outputs were regridded (via bilinear interpolation) to a uniform $1^\circ \times 1^\circ$ grid using the xESMF Python package (Zhuang et al., 2021), but transport calculations were performed on each model’s native grid (Sect. 2.2.4). The pre-industrial simulations were used to remove the linear control drifts from all scalar fields (oxygen, salinity, temperature, ideal age, export)

in the historical and SSP5-8.5 simulations using the xMIP Python package (Busecke and Spring, 2020).

We also use the observational climatology of dissolved oxygen concentrations from the World Ocean Atlas 2018 (WOA18; Garcia et al., 2019) to evaluate the representation of the Indian Ocean OMZ and dissolved oxygen field in the ensemble of ESMs. We use an average over the period of 1950–2015 in the historical simulations to compare to the observed climatology.

2.2 Analysis

To characterize the response of ocean variables to climate change, we used linear trends over the 2015–2100 period in the SSP5-8.5 simulations (normalized to change per century), except when calculating water mass fractions (Sect. 2.2.3), for which we compare historical (1950–2015 average) and end-of-century (historical plus integrated linear trend over 85 years) states. To represent the ESM ensemble, we take the mean over models (multi-model mean) and use 1 standard deviation of the model spread on either side of the mean as a measure of uncertainty. When presenting multi-model mean trend fields, we stipple where less than 75 % of available models agree on the sign of change to indicate regions of uncertainty. While we perform our analysis over the full water column, we focus on thermocline depths (upper 1000 m) so that the results may characterize impacts on mesopelagic ecosystems. When examining oxygen and ideal age trends, we exclude surface waters by examining changes between 100 and 1000 m.

2.2.1 Tracking ocean volume by oxygen threshold

OMZ volume is generally defined as the volume of water below a chosen oxygen concentration threshold. We extend this idea to a wide range of oceanic oxygen concentration values. Here, we define the full-column OMZ volume as a function of oxygen thresholds, $O_{2,T}$ (following Busecke et al., 2022):

$$\mathcal{V}_{O_2}(O_{2,T}) = \int \int \int_{O_2 \leq O_{2,T}} dV, \quad (1)$$

where we integrate over the Indian Ocean from 30°S – 25°N and from the African continent to the west to Indonesia and Australia, extending to about 125°E in the main strait of the Indonesian Throughflow (Timor Sea), to the east. The Red Sea and Persian Gulf are not included in the integration of \mathcal{V}_{O_2} . We use the Equator to delimit the Arabian Sea and Bay of Bengal sub-basins to the south. However, we do not focus on the full OMZ volume but rather on the thermocline OMZ volume.

$$\mathcal{V}_{O_2}^{1000}(O_{2,T}) = \int_0^{1000 \text{ m}} \int \int_{O_2 \leq O_{2,T}} dV \quad (2)$$

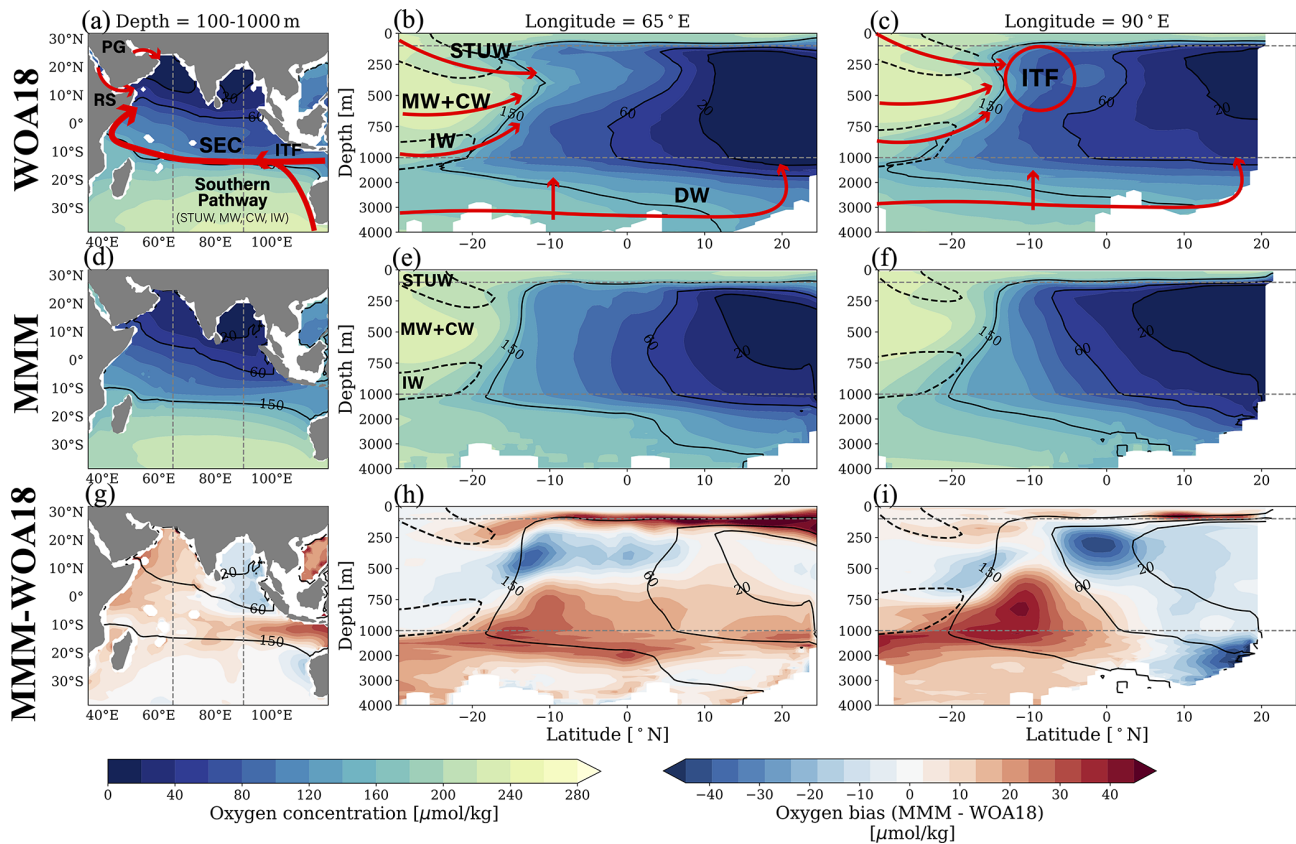


Figure 1. Dissolved oxygen annual mean climatology from the World Ocean Atlas 2018 (WOA18) (a) averaged between 100 and 1000 m, (b) at 65° E, and (c) at 90° E. Multi-model mean (MMM) dissolved oxygen in the Indian Ocean for the historical period (1950–2015) (d) between 100 and 1000 m, (e) at 65° E, and (f) at 90° E. Difference between MMM (1950–2015) and WOA18 dissolved oxygen (g) between 100 and 1000 m, (h) at 65° E, and (i) at 90° E. Solid black contours represent 20, 60, and 150 $\mu\text{mol kg}^{-1}$ oxygen in (a–c) WOA18 and (d–i) MMM. (a, d, g) Dashed gray lines indicate 65° E and 90° E. (b, c, e, f, h, i) Dashed gray lines indicate depths of 100 and 1000 m, and dashed black contours are salinity contours highlighting Subtropical Underwater and Intermediate Water. Water masses and ventilation pathways are illustrated schematically. Abbreviations: South Equatorial Current (SEC), Central Water (CW), Deep Water (DW), Subtropical Underwater (STUW), Mode Water (MW), Intermediate Water (IW), Indonesian Throughflow (ITF).

Table 1. ESM data used in this study. Variables used: dissolved oxygen concentration (o2), salinity (so), potential temperature (thetao), ideal age (agesc), export of organic carbon at 100 m (epc100), and mass transport (umo/vmo) where available. All data used in this study are publicly available via ESGF, except ideal age fields from GFDL-CM4 and GFDL-ESM4 (see Busecke et al., 2022).

ESM	Variables	Member ID
GFDL-CM4 (Guo et al., 2018a, b)	o2, thetao, so, agesc	rli1p1f1
GFDL-ESM4 (Krasting et al., 2018; John et al., 2018)	o2, thetao, so, agesc, epc100	rli1p1f1
MIROC-ES2L (Hajima et al., 2019; Tachiiri et al., 2019)	o2, thetao, so, agesc, epc100	rli1p1f2
MPI-ESM1-2-HR (Jungclaus et al., 2019; Schupfner et al., 2019)	o2, thetao, so, epc100, umo/vmo	rli1p1f1
MPI-ESM1-2-LR (Wieners et al., 2019a, b)	o2, thetao, so, agesc, epc100, umo/vmo	rli1p1f1
NorESM2-LM (Seland et al., 2019a, b)	o2, thetao, so, agesc, epc100, umo/vmo	rli1p1f1
NorESM2-MM (Bentsen et al., 2019a, b)	o2, thetao, so, agesc, epc100, umo/vmo	rli1p1f1
UKESM1-0-LL (Tang et al., 2019; Good et al., 2019)	o2, thetao, so, epc100, umo/vmo	rli1p1f2

Note that we integrate over the upper 1000 m here, rather than 100 to 1000 m, because OMZ volume will naturally exclude surface waters. In both cases, we use oxygen thresholds $O_{2,T}$ that vary between 5 and $225 \mu\text{mol kg}^{-1}$ and highlight three benchmark thresholds: (1) $O_{2,T} = 20 \mu\text{mol kg}^{-1}$ (OMZ20) as the core of the OMZ, (2) $O_{2,T} = 60 \mu\text{mol kg}^{-1}$ (OMZ60) as a commonly cited threshold for hypoxia at which marine ecosystems tend to experience significant loss of biodiversity (Vaquer-Sunyer and Duarte, 2008), and (3) $O_{2,T} = 150 \mu\text{mol kg}^{-1}$ (OMZ150) as a common habitat boundary for large commercial fish species such as tuna (Brill, 1996; Prince and Goodyear, 2006; Bertrand et al., 2011; Stramma et al., 2012; Brill, 1994). We note that oxygen thresholds above $150 \mu\text{mol kg}^{-1}$ are not generally used to delimit low-oxygen environments and OMZs, but we present them here to provide a holistic view of forced changes in oxygen distribution.

2.2.2 Thermal and non-thermal dissolved oxygen trends

We separate the influences of thermal and non-thermal processes on oxygen trends. The thermal component, or oxygen saturation O_{2SAT} , is calculated using the GSW Python package from potential temperature and salinity fields (Firing et al., 2021). The non-thermal component, related to ocean ventilation and biological sources and sinks of oxygen, is computed as the residual between O_2 and O_{2SAT} and is referred to as apparent oxygen utilization (AOU).

$$O_2 = O_{2SAT} - \text{AOU} \quad (3)$$

We compute O_{2SAT} and AOU for each year in the historical and SSP5-8.5 simulations, then take historical means and projected linear trends. Trends in AOU represent the contribution of non-thermal processes to overall changes in dissolved oxygen, but they encompass changes in both physical (ventilation changes tied to slower circulation or changes in mixing) and biological (respiration rates) effects. We use the ideal age of seawater (i.e., the time since exposure to the surface) to qualitatively infer the contribution of physical ventilation changes.

2.2.3 Identifying changes in ventilation pathway contributions

In Sect. 3.5 and 3.6, we solve a mixture model in the South Equatorial Current and in the Arabian Sea to evaluate shifts in water mass fractions under SSP5-8.5 forcing. The mixture model is based on extended optimum multiparameter analysis (OMP) (Tomczak, 1981; Tomczak and Large, 1989; Karstensen and Tomczak, 1998). This technique solves for the water mass fractions at a given hydrographic section using the hydrographic properties of specified source water mass types, each representing an advective ventilation pathway. See Appendix A and references therein for details on the

method and how the mixture model implemented here differs from classical OMP. We use a Python implementation (py-OMPA; Shrikumar et al., 2022) based on the original MATLAB code from Karstensen and Tomczak (1998). We perform this analysis along potential density surfaces referenced to zero pressure (σ_0), calculated from potential temperature and salinity fields using the GSW Python package (Firing et al., 2021). For each region, we use a nominal value for potential density that captures features of significant dissolved oxygen change; however, we tune this value (within 0.5) for individual ESMs to better capture features across models.

The number of source water mass types is limited to be less than or equal to the number of hydrographic properties available. Here, we use potential temperature, salinity, dissolved oxygen, and AOU. To account for remineralization along the pathways (between source and case study regions), we allow for the conversion of dissolved oxygen to AOU (see Appendix A for details). In the case of the South Equatorial Current region, the source water types are Indonesian Throughflow Water, Southern Pathway Waters, and Arabian Sea Water, centered at (15°S , 120°E), (30°S , 100°E), and (15°N , 65°E), respectively, at a nominal potential density of $\sigma_0 = 26.4$. In the case of the Arabian Sea, the source waters are Persian Gulf Water, Red Sea Outflow Water, and Arabian Sea Water centered at (24.5°N , 58.5°E), (12°N , 47°E), and (15°N , 65°E), respectively, at a nominal potential density of $\sigma_0 = 25.7$. We exclude MIROC-ES2L from the mixture model analysis in the Arabian Sea because the model does not resolve the Persian Gulf and Red Sea. To account for the sensitivity of results to small changes in the sampling of source water types and potential density layer, we average 50 realizations of the experiment by applying random perturbations to source water locations and density layers from their central values. Source water locations are perturbed by up to 5° in latitude and longitude for the South Equatorial Current region and 2° for the Arabian Sea. For both locations, the value of the potential density layer is perturbed by up to 0.1 kg m^{-3} .

For each ESM in the ensemble, we solve for the water mass fractions, f , for a historical state and an end-of-century state. For the historical state, we first compute potential density for the historical mean (1950–2015) for each ESM and use the `xgcm` (Abernathey et al., 2022) package to transform the vertical coordinates of each model to potential density space. We note that the results of the mixture model are not sensitive to the order of operations (temporal averaging and vertical transformation). To compute an end-of-century state, we add 85-year (2015–2100) forced trends from the SSP5-8.5 simulations to historical mean fields (potential temperature, salinity, oxygen, AOU) to represent a climatological year 2100, then repeat the coordinate transformation described above.

From the mixture model results, we quantify the change in oxygen supply due to shifts in water mass composition and

properties for key regions:

$$\Delta O_{2,\text{supply}} = \sum_i f_{i,1} O_{i,1} - \sum_i f_{i,0} O_{i,0}, \quad (4)$$

where f_i and O_i are the fraction and oxygen concentration of source water type i for future (1) and historical (0) states. We compare $\Delta O_{2,\text{supply}}$ to the total simulated changes in oxygen to evaluate how well changes in the system can be described by only isopycnal transport and mixing of source water mass types. While for conservative tracers (i.e., potential temperature and salinity) the change in supply and total change should be equal if the system is well represented by the mixture model analysis, an allowance for the remineralization of oxygen can lead to an imbalance between the two quantities (see Appendix A).

A concern when solving for forced trends on a potential density layer is that the results may be influenced by the displacement of this isopycnal in depth. Indeed, the potential density layers chosen here are displaced deeper in the water column by about 100 m between the historical and end-of-century states. To evaluate the impact of this deepening, we perform an alternate set of mixture model experiments where we use a lower density value at the end-of-century state than for evaluating the historical state. The layer defined by this lower density value samples the same depth as was sampled for the historical state. The results of this alternative analysis, presented in the Supplement, are qualitatively similar to the analysis presented in the main text and do not change the main results.

2.2.4 Quantifying changes in transport by ventilation pathways

To provide context for trends in dissolved oxygen and ideal age, we quantify changes in individual thermocline ventilation pathways using mass transport fields on each model's native grid. The Indonesian Throughflow Water transport is calculated as the westward flow through the main strait of the Indonesian Throughflow at 114° E integrated between 100 and 1000 m. The Southern Pathway Water transport is calculated as the northward flow across 30° S integrated between 100 and 1000 m. We note that this representation of Southern Pathway Waters largely excludes the contribution of Subtropical Underwater, which subducts north of 30° S. The upwelling of Deep Waters into the thermocline is calculated as the budget residual of transport below 1000 m across 30° S and through the Indonesian Throughflow at 114° E. Transports by marginal sea outflows from the Red Sea and Persian Gulf are defined as the outflowing components through their respective channels. We report transport trends in sverdrups (Sv) per century using a constant reference density of 1025 kg m⁻³ to convert between mass and volume transport. Transport fields are available for five of the eight ESMs in the ensemble (MPI-ESM1-2-HR, MPI-ESM1-2-LR, NorESM2-LM, NorESM2-MM, UKESM1-0-LL).

3 Results

3.1 Historical oxygen and ventilation pathways in observations and Earth system models

The observed oxygen distribution in the Indian Ocean thermocline (100 to 1000 m) is influenced by five main ventilation pathways (Fig. 1a–c). First, the Southern Pathway Waters which enter via the southern Indian Ocean gyre include (from least to most dense) Subtropical Underwater (STUW; about 100 to 250 m depth), Indian Central Water and Subantarctic Mode Water (CW+MW; about 250 to 750 m depth), and Antarctic Intermediate Water (IW; about 750 to 1000 m depth) (Sprintall and Tomczak, 1993; Karstensen and Tomczak, 1997; McCarthy and Talley, 1999; Karstensen and Quadfasel, 2002; Fine, 1993; Talley, 2011). This spectrum of waters enters the basin with a range of oxygen between about 160 and 250 $\mu\text{mol kg}^{-1}$, where Indian Central Water and Subantarctic Mode Water account for the highest oxygen levels. Southern Pathway Waters are capped by the salinity maximum of Subtropical Underwater and the salinity minimum of Antarctic Intermediate Water (dashed black contours in Fig. 1b and c). Second, the Indonesian Throughflow (ITF) brings waters from the tropical Pacific Ocean (with oxygen concentrations of about 80–170 $\mu\text{mol kg}^{-1}$ between 100 and 1000 m depth) into the southern Indian Ocean which mix with Southern Pathway Waters in the South Equatorial Current (SEC). This mixture of waters then crosses the Equator with the western boundary current to ventilate the northern basin (pathway schematic in Fig. 1a) via eddy mixing, monsoonal currents, and the weak North Equatorial Current which flows east in the summer along about 5° N (Schott et al., 2009; Phillips et al., 2021; Resplandy et al., 2012; Lachkar et al., 2016). In the northern Indian Ocean, two additional pathways are associated with saline marginal sea outflows: Red Sea Outflow Water (RS, with concentrations around 70 $\mu\text{mol kg}^{-1}$) and Persian Gulf Water (PG, near oxygen saturation > 200 $\mu\text{mol kg}^{-1}$) deliver oxygen directly to the OMZ core in the Arabian Sea as they are quickly diluted by mixing (Fig. 1a). Finally, the fifth pathway corresponds to Deep Waters (DWs) that enter from the Southern Ocean and Indonesian Throughflow (here taken as waters below 1000 m depth) and slowly upwell in the basin (McCarthy et al., 1997), ventilating the thermocline from below with relatively well-oxygenated waters (100–200 $\mu\text{mol kg}^{-1}$).

The multi-model mean (eight ESMs; see the Methods section) captures the main features associated with the five pathways ventilating the Indian Ocean (Fig. 1d–f). The multi-model mean simulates the full spectrum of Southern Pathway Waters, indicated by the salinity maximum and minimum associated with Subtropical Underwater and Antarctic Intermediate Water (dashed black contours in Fig. 1e and f), and overall captures the temperature and salinity properties of water masses across the basin (Fig. S5). We note that three of the eight ESMs simulate the Southern Pathway Waters par-

ticularly well (GFDL-CM4, GFDL-ESM4, and UKESM1-0-LL), while three others are missing the salinity minimum associated with Antarctic Intermediate Water (MIROC-ES2L, MPI-ESM1-2-HR, and MPI-ESM1-2-LR, Fig. S4). The oxygen supply from the Southern Pathway and the Indonesian Throughflow is also relatively well simulated by the multi-model mean (Fig. 1a–c), and the observed oxygen maximum associated with Indian Central Water and Subantarctic Mode Water is present in all the ESMs in the ensemble (though it is weaker than observed in MPI-ESM1-2-HR and MPI-ESM1-2-LR, see Figs. S3 and S4). Overall, these simulated thermocline ventilation pathways maintain a realistic meridional oxygen gradient with well-oxygenated waters in the southern basin and OMZ cores in the Arabian Sea and Bay of Bengal (contours of 20, 60, and 150 $\mu\text{mol kg}^{-1}$ water extent shown in solid black contours in Figs. 1 and S4). There are, however, significant biases in the oxygen field simulated in the northern basin where the multi-model mean simulates higher than observed oxygen levels in the Arabian Sea and lower than observed in the Bay of Bengal (Figs. 1g–i and S3). The high oxygen bias in the Arabian Sea is likely due to excessive ventilation from marginal seas and southern source waters, though it may also be influenced by deficiencies in parameterized oxygen consumption rates and eddy mixing rates (Schmidt et al., 2021), while the low oxygen bias in the Bay of Bengal is possibly tied to the overestimation of oxygen consumption rates and remineralization depths (Al Azhar et al., 2017). These are well-documented biases among ESMs (Oschlies et al., 2008; Bopp et al., 2013; Rixen et al., 2020; Schmidt et al., 2021). However, we have mitigated oxygen biases in the Arabian Sea in our ensemble by removing models that lack suboxia there (Sect. 2.1 and Fig. S6).

We compare thermocline OMZ volume ($\mathcal{V}_{\text{O}_2^{1000}}$, volume in upper 1000 m) in observations and the multi-model mean for oxygen thresholds between 5 and 225 $\mu\text{mol kg}^{-1}$ (Fig. 2a, $\mathcal{V}_{\text{O}_2^{1000}}$ for individual models are in Table S1). In the observed climatology, $\mathcal{V}_{\text{O}_2^{1000}}$ increases about linearly with oxygen threshold, with a hypoxic volume OMZ60 ($< 60 \mu\text{mol kg}^{-1}$) of about $8.3 \times 10^{15} \text{ m}^3$ and a low oxygenated water volume OMZ150 ($< 150 \mu\text{mol kg}^{-1}$) of about $21 \times 10^{15} \text{ m}^3$. The multi-model mean simulates this linear relationship. In particular, it agrees with observations within 12 % for the OMZ60 volume and within 7 % for the OMZ150 volume, and at both benchmarks the observations fall within the ensemble spread with no clearly outlying ESM. The volume of the core OMZ20, however, is overestimated by about 50 % in the multi-model mean. The good agreement at hypoxic and higher thresholds arises from the realistic simulation of the southern Indian Ocean ventilation pathways that control these volumes. In contrast, the disagreement in the volume of the OMZ core primarily comes from the systematic overestimation of OMZ20 in the Bay of Bengal, a bias only partially offset by the underestimation of OMZ20 in the Arabian Sea (Fig. 2b and c).

3.2 Projected OMZ volume exhibits diverging trends at low and high oxygen thresholds

Projections of thermocline OMZ volume under SSP5-8.5 forcing fall into three regimes: a robust expansion of volumes set by high oxygen thresholds (above 180 $\mu\text{mol kg}^{-1}$), a robust contraction of volumes set by low oxygen thresholds (below 85 $\mu\text{mol kg}^{-1}$), and a transition regime with weak and uncertain trends characterized by redistribution of volume (between 85 and 180 $\mu\text{mol kg}^{-1}$; Fig. 3a). We define robust OMZ expansion and contraction as where the multi-model mean trends exceed 1 standard deviation of the model spread. The volumes of hypoxic waters (OMZ60) and core waters (OMZ20) contract at similar rates in the multi-model mean ($0.7 \pm 0.4 \times 10^{15}$ and $0.8 \pm 0.7 \times 10^{15} \text{ m}^3$ per century, respectively). The model spread is tighter for trends in OMZ20, so the multi-model mean signal of volume trends emerges in the ensemble earlier for OMZ20 than for OMZ60 (Fig. 3b and c). About half of the OMZ20 contraction occurs in the Arabian Sea (Fig. S8). Meanwhile, the volume of OMZ150 falls between the regimes of robust expansion and contraction and experiences near-zero volume changes in the multi-model mean by 2100. Tracking the evolution of the OMZ150, we see that ESMs project an expansion over the historical period and first half of the twenty-first century before disagreeing on the trajectory in the latter half of the century, with half of the ESMs projecting a contraction by 2100 (GFDL-CM4, MPI-ESM1-2-LR, UKESM1-0-LL, MIROC-ES2L) and the other half projecting an expansion (GFDL-CM4, MPI-ESM1-2-HR, NorESM2-LM, NorESM2-MM; Fig. 3d). Lastly, the volume of waters with less than 200 $\mu\text{mol kg}^{-1}$ evolves similarly to the volume of the OMZ150 over the historical period but then continues to follow a trajectory of robust expansion over the twenty-first century (Fig. 3e).

3.3 Regional contrasts in dissolved oxygen trends reshape the Indian Ocean OMZ

Projected trends in dissolved oxygen are highly variable in space, both horizontally and vertically, leading to regional contraction, expansion, and redistribution of the OMZ volume (Fig. 4). The multi-model mean projects a weak increase in oxygen in the OMZ cores of the Arabian Sea and Bay of Bengal and a decline in oxygen in the relatively well-oxygenated water masses entering via the Southern Pathway (Fig. 4). Strongest oxygen changes, however, are found at intermediate oxygen levels. We focus on the three major features that influence the OMZ volume at these intermediate levels (labeled by numbers in Fig. 4): the deoxygenation in the southeastern basin (Feature 1), the oxygenation of the western South Equatorial Current (Feature 2), and the deoxygenation in the northern Arabian Sea (Feature 3). Feature 1 coincides with the flow of Southern Pathway Waters in the subtropical gyre and Indonesian Throughflow Water entering the Indian Ocean. Indeed, we see two distinct max-

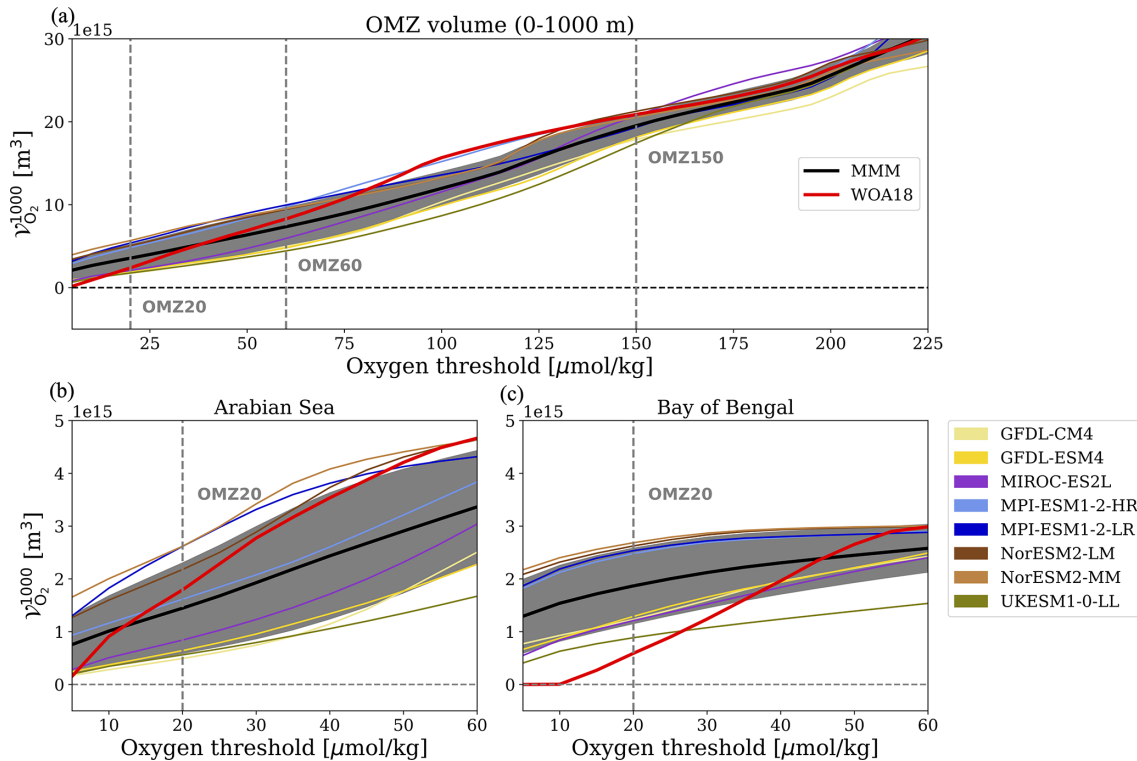


Figure 2. OMZ volume taken between 0 and 1000 m in the (a) Indian Ocean and sub-basins (b) in the Arabian Sea and (c) Bay of Bengal for the multi-model mean averaged over 1950–2015 (MMM; black) and observed climatology (WOA18; red). Shading represents 1 standard deviation of the model spread from the mean. Individual ESMs are shown in colored curves.

ima of the deoxygenation along the meridional section at 90° E (Fig. 4c): one coinciding with Southern Pathway Waters (namely Central, Mode, and Intermediate Waters) centered around 500 m depth with deoxygenation rates up to 35 $\mu\text{mol kg}^{-1}$ per century and one coinciding with Indonesian Throughflow Waters at around 250 m depth with deoxygenation rates up to 50 $\mu\text{mol kg}^{-1}$ per century. Feature 2 is located where Southern Pathway Waters and Indonesian Throughflow Waters mix within the South Equatorial Current. Feature 2 has a maximum oxygenation trend in the South Equatorial Current between 100 and 500 m, where waters oxygenate at a rate of up to about 50 $\mu\text{mol kg}^{-1}$ per century, and a secondary maximum in the North Equatorial Current, with oxygenation rates up to 40 $\mu\text{mol kg}^{-1}$ per century (Fig. 4a and b). Together, Features 1 and 2 form an oxygenation–deoxygenation dipole along the path of the South Equatorial Current. Lastly, Feature 3 is deoxygenation at a rate of up to about 60 $\mu\text{mol kg}^{-1}$ per century in the northern Arabian Sea between about 100 and 300 m depth, a region where the Persian Gulf Outflow (observed down to about 400 m depth) and winter convection (observed mixed layers down to about 100 m depth) dominate ventilation (Fig. 4a and b).

The three features of dissolved oxygen trends are simulated by all individual ESMs in the ensemble (Figs. S9

and S10), leading to a robust pattern in the multi-model mean (more than 75 % of models agree on sign of trend; Fig. 4). However, there are some notable differences in their amplitude and extent across the ensemble. Here, we leverage comparisons between models that share the same architecture but differ either in their horizontal resolution or the complexity of their biogeochemical module to illustrate the sensitivity of the oxygen response to the model characteristics. For example, GFDL-CM4 and GFDL-ESM4 have the same dynamical ocean model but differ in both oceanic and atmospheric resolution (GFDL-CM4 has higher resolution) as well as biogeochemical components (GFDL-ESM4 has more complex representation of biogeochemistry) (Dunne et al., 2020; Held et al., 2019). Despite very similar historical representations of oxygen in the Indian Ocean, GFDL-CM4 and GFDL-ESM4 simulate different strengths of oxygenation in the SEC (Feature 2) and deoxygenation in the Arabian Sea (Feature 3), with GFDL-CM4 projecting more pronounced features in both regions (Fig. S10). Meanwhile, NorESM2-LM and NorESM2-MM, which differ only in the horizontal resolution of their atmospheric components (Seland et al., 2020), project similar trends for oxygenation in the SEC but differ on the strength of the deoxygenation in the Arabian Sea, with weaker deoxygenation simulated in the higher-atmospheric-resolution version (NorESM2-MM; Fig. S10).

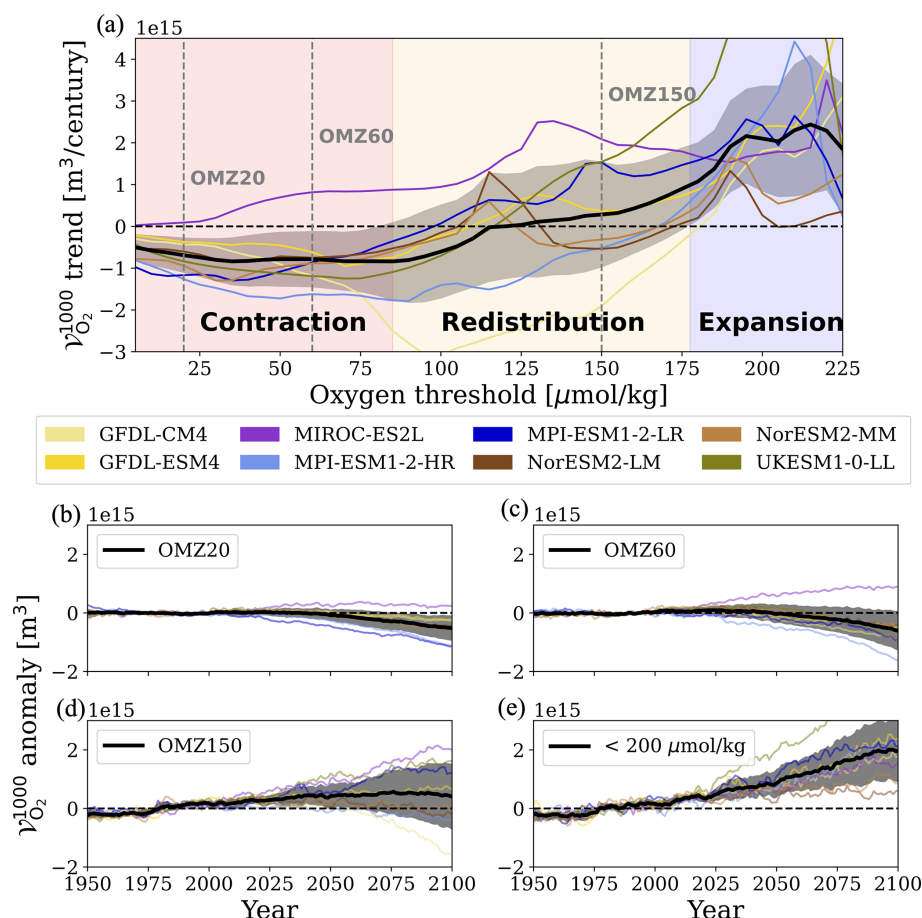


Figure 3. Multi-model mean thermocline OMZ volume changes (between 0 and 1000 m) under SSP5-8.5 scenario forcing (2015–2100). (a) $V_{O_2}^{1000}$ trends as a function of oxygen threshold for the Indian Ocean. The 20, 60, and 150 $\mu mol kg^{-1}$ thresholds bounding OMZ20, OMZ60, and OMZ150 are indicated with gray dashed lines. Time series of the $V_{O_2}^{1000}$ anomaly from 1950–2100 (anomaly referenced to 1950–2015 mean) for (b) OMZ20, (c) OMZ60, and (d) OMZ150, as well as (e) waters with $< 200 \mu mol kg^{-1}$ oxygen. Shading represents 1 standard deviation of model spread from the mean.

Finally, CanESM5 and CanESM5-CanOE only differ in the complexity of their biogeochemical model (Christian et al., 2022). Both CanESM models were removed from our multi-model mean due to the absence of suboxia in the Arabian Sea, but we use them here to illustrate the sensitivity to the biogeochemical complexity. CanESM5-CanOE, which has a more complex representation of biogeochemistry, projects weaker oxygenation in the SEC and stronger deoxygenation in the Arabian Sea than the simpler CanESM5 model. These results suggest that the sign of oxygen change is robust across the ensemble but that both model resolution (atmospheric and oceanic) and biogeochemical complexity influence the amplitude of the change.

These three features ultimately explain the contraction, expansion, and redistribution of the OMZ volume at thermocline depths across oxygen thresholds. The deoxygenation of the southeastern basin (Feature 1) is the primary driver of the volume expansion at high oxygen thresholds ($>$

180 $\mu mol kg^{-1}$, Fig. 3b). The oxygenation–deoxygenation dipole (from Features 1 and 2) redistributes the OMZ volume from west to east and explains the weak volume changes found at intermediate oxygen thresholds (between 85 and 180 $\mu mol kg^{-1}$) including the volume of the OMZ150 (redistribution regime, Fig. 3b). The oxygenation in the South Equatorial Current, and in turn the western boundary current waters (Feature 2), contributes to the OMZ contraction at low oxygen thresholds including the volume of OMZ60 (contraction regime, Fig. 3b), although the net change in volume is relatively small due to the compensating expansion in the northern Arabian Sea which also affects the low oxygen thresholds (Feature 3).

3.4 Dissolved oxygen trends are dominated by changes in ventilation

To identify which processes control projected dissolved oxygen trends and in turn the reshaping of the Indian

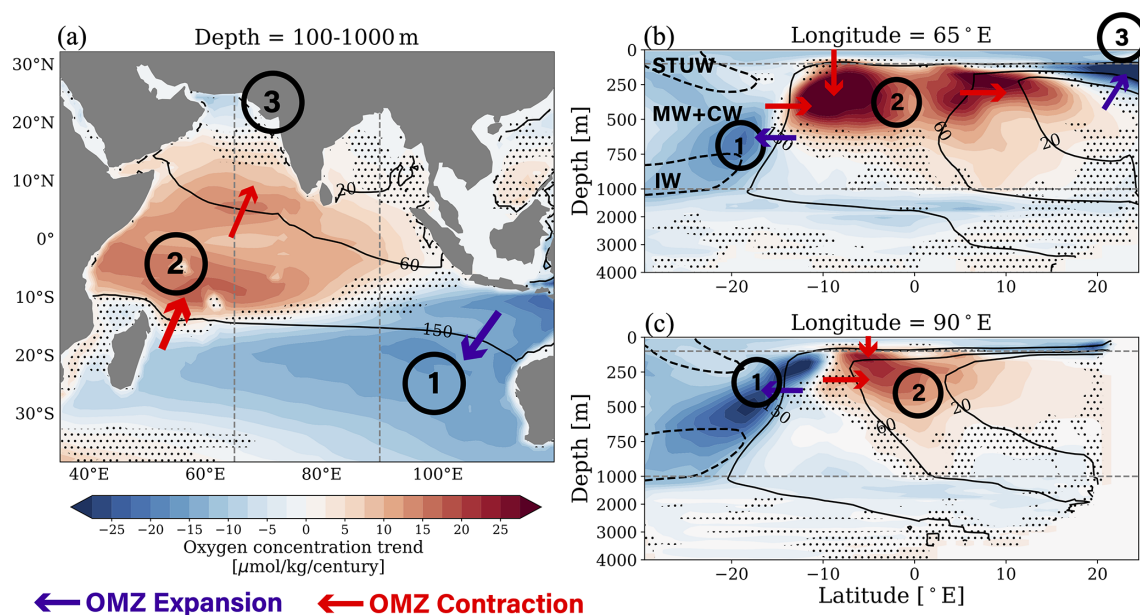


Figure 4. Multi-model mean (MMM) dissolved oxygen trends under SSP5-8.5 scenario forcing (2015–2100). Dissolved oxygen trends (a) between 100 and 1000 m, (b) at 65° E, and (c) at 90° E. Dashed gray lines mark (a) 65° E and 90° E, and panels (b, c) show 100 and 1000 m. Solid black contours represent 20, 60, and 150 $\mu\text{mol kg}^{-1}$ oxygen. Dashed black contours highlight salinity signatures of Subtropical Underwater (STUW) and Intermediate Water (IW), with Central Water (CW) and Mode Water (MW) between. Main features of dissolved oxygen trends are numbered, with an effect on OMZ volume indicated by purple and red arrows. Results are stippled where less than 75 % (six out of eight) of models agree on the sign of the trend.

Ocean OMZ, we separate dissolved oxygen trends into thermal and non-thermal components (Fig. 5). Thermal oxygen trends relate to changes in oxygen saturation concentrations, while non-thermal oxygen trends arise from changes in physical ocean circulation and biological respiration rates (Sect. 2.2.2). Thermal and non-thermal effects tend to influence different water masses: thermal trends are strongest in surface waters (above 100 m), while non-thermal trends are strongest at thermocline depths (100 to 1000 m) but are also responsible for deoxygenation in the deep ocean (below 1000 m) (Fig. 5). Thermal oxygen changes drive relatively uniform deoxygenation in the surface ocean of about 5 to 15 $\mu\text{mol kg}^{-1}$ per century. Thermal effects are only significant below 100 m along the pathways of Subtropical Underwater (Fig. 5b) and Indonesian Throughflow Water (Fig. 5a and c). The non-thermal component largely explains the strong patterns of oxygenation and deoxygenation discussed above, including deoxygenation in the southeast, oxygenation in the SEC, and deoxygenation in the northern Arabian Sea (Features 1 to 3; Figs. 4 and 5d–f).

The ideal age of seawater, or the average time since water has been exposed to the surface, is a direct measure of ventilation timescale; trends in ideal age thus indicate changes in the rate of ventilation from advection and mixing. Trends in ideal age agree with the pattern of non-thermal oxygen trends. The regions of maximum decreased ventilation (i.e., waters get older) spatially correspond to deoxy-

genation in the southeastern basin (Feature 1) and Arabian Sea (Feature 3), while the region of maximum increased ventilation (i.e., waters get younger) corresponds to the region of oxygenation in the South Equatorial Current (Feature 2; Figs. 5g–i and S11). This suggests that changes in physical ventilation pathways are the main control of features of dissolved oxygen change and ultimately the reshaping of OMZ volume in the Indian Ocean.

3.5 Shifts in water mass composition control oxygenation in South Equatorial Current

In this and the following section, we attribute the significant features of projected oxygen trends in the Indian Ocean thermocline to specific changes in ventilation pathways. Perhaps the most remarkable aspect of projected dissolved oxygen changes in the Indian Ocean under SSP5-8.5 forcing is the oxygenation–deoxygenation dipole along the South Equatorial Current (SEC) (Features 1 and 2). The two major ventilation pathways in this region are the Southern Pathway Waters and Indonesian Throughflow Water. The transport of these two pathways is projected to decline between 100 and 1000 m over the twenty-first century (Fig. S12). The transport of Southern Pathway Water across 30° S is projected to decline by 4.4 ± 3.2 Sv per century (from 53 ± 2 Sv) and the transport of Indonesian Throughflow Water by 5.1 ± 2.0 Sv per century from (15 ± 3) Sv). The weakening of these transport pathways can explain the deoxygenation in the south-

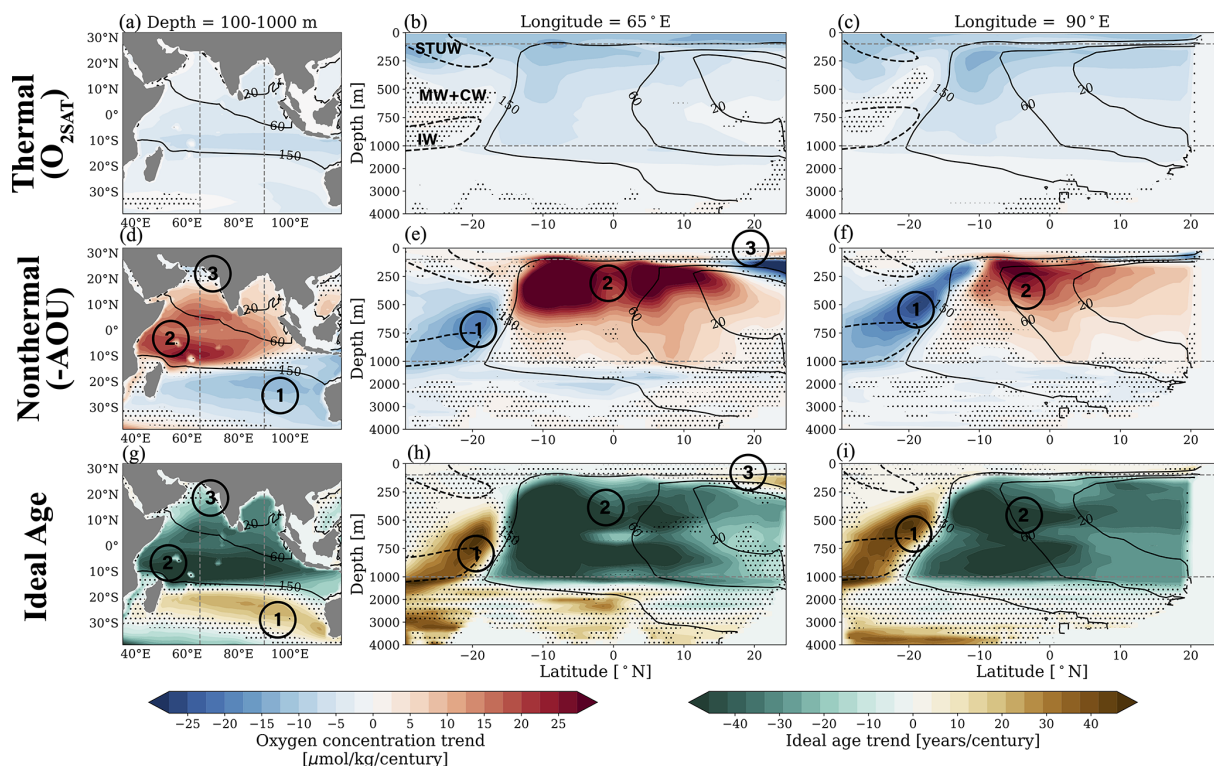


Figure 5. Thermal and non-thermal components of multi-model mean (MMM) dissolved oxygen trends under SSP5-8.5 scenario forcing (2015–2100). Thermal oxygen (O_{2SAT}) trends (a) between 100 and 1000 m, (b) at 65° E, and (c) at 90° E. Non-thermal oxygen (AOU) trends (d) between 100 and 1000 m, (e) at 65° E, and (f) at 90° E. Multi-model mean (MMM) ideal age trends (g) between 100 and 1000 m, (h) at 65° E, and (i) at 90° E. Dashed gray lines mark (a, d) 65° E and 90° E, and panels (b, c, e, f, h, i) show 100 and 1000 m. Solid black contours represent 20, 60, and $150 \mu\text{mol kg}^{-1}$ oxygen. Dashed black contours represent salinity contours highlighting Subtropical Underwater (STUW) and Intermediate Water (IW), with Central Water (CW) and Mode Water (MW) between. Main features of dissolved oxygen trends are numbered. Results are stippled where less than 75 % (six out of eight) of models agree on the sign of the trend.

eastern Indian Ocean where each pathway acts as a single dominant source (thus accounting for Feature 1). Curiously, however, this weakened transport seems in apparent contradiction with the increased ventilation and oxygenation of the western SEC (Fig. 4). We hypothesize that this oxygenation must arise from a shift in the relative contributions between these source waters in the western SEC where they co-dominate, favoring relatively young and oxygen-rich waters from the Southern Pathway over relatively old and oxygen-poor waters from the Indonesian Throughflow. To test this hypothesis, we perform a mixture model analysis (Tomczak and Large, 1989) in the tropical Indian Ocean for both a historical mean state (1950–2015) and an end-of-twenty-first-century mean state (climatological 2100) at a potential density layer within the thermocline, nominally $\sigma_0 = 26.4$ (Sect. 2.2.3). This potential density layer intersects the dipole of oxygen change (Features 1 and 2) in the South Equatorial Current (Fig. 6a). We solve for the fractions of three source waters: Indonesian Throughflow Water, Southern Pathway Water and Arabian Sea Water (oxygen minimum water; Sect. 2.2.3). We find that the mixture model analysis is able to reconstruct historical and future oxygen,

temperature, and salinity in this region with composites of source water types (see Fig. S13 for a comparison of simulated and reconstructed states in the Feature 2 region).

In the multi-model mean historical state, the mixture model analysis highlights Indonesian Throughflow Water originating from the main straits of the Indonesian Throughflow and penetrating across the basin along 10° S, as well as Southern Pathway Water residing primarily within the southern gyre until it joins the western boundary current (Fig. 6b; in agreement with observed distribution from Tomczak and Large, 1989). Specifically, the mixture model suggests that waters in the region of Feature 2 in the western SEC are composed of about 40 % Indonesian Throughflow Water, 30 % Southern Pathway Water, and 30 % Arabian Sea Water in the multi-model mean (average composition between 40° – 80° E and 5° – 15° S, Fig. 6b). Under SSP5-8.5 forcing, there is a significant shift in water mass fractions in the western SEC away from Indonesian Throughflow Water in favor of Southern Pathway Water between the historical and future states. By the end of the century, the composition of this region is projected to shift to about 20 % Indonesian Throughflow Water and 55 % Southern Pathway Water (changes of -0.2 and

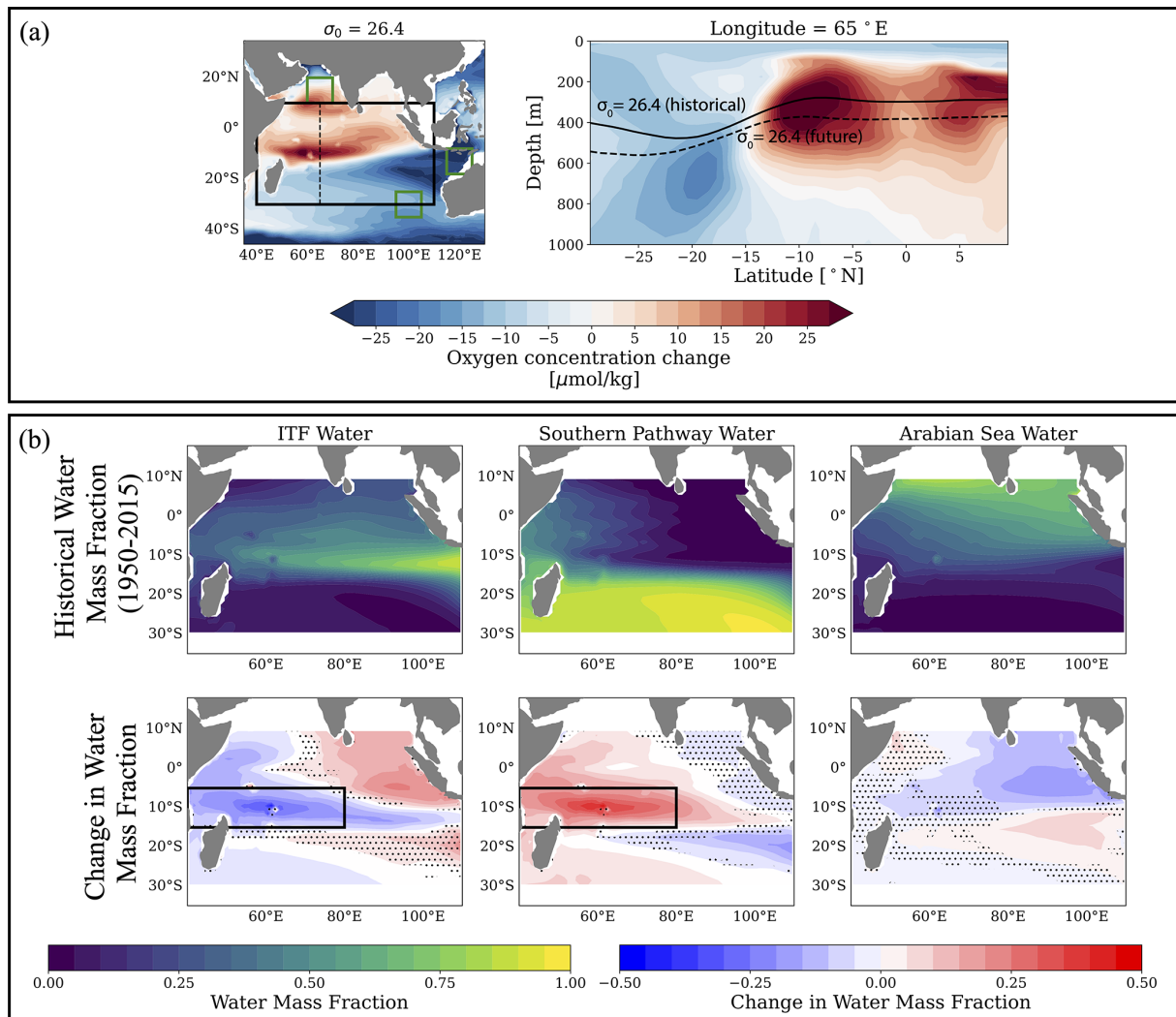


Figure 6. Multi-model mean (MMM) results of mixture model analysis in the South Equatorial Current (SEC). (a) Oxygen changes along the $\sigma_0 = 26.4$ surface and the historical (solid) and end-of-century (dashed) depth of $\sigma_0 = 26.4$ indicated over MMM oxygen changes in depth space at 65°E . Green boxes mark source water regions, and the solid black box represents the region for which water mass fractions are solved. (b) Historical distribution of Indonesian Throughflow, Southern Pathway, and Arabian Sea Water fractions, as well as changes in water mass fractions between historical and end-of-century states. Historical states are calculated as a 1950–2015 mean, and end-of-century states are calculated as a historical mean plus linear trends over 2015–2100. Solid black boxes in (b) show the region of the western SEC. Stippling shows where less than 75 % (six out of eight) of models agree on the sign of change.

+0.25 water mass fractions for Indonesian Throughflow and Southern Pathway Waters, respectively), while the contribution of Arabian Sea Water stays relatively constant (Fig. 6b).

In all ESMs except one (MPI-ESM1-2-LR), the simulated oxygenation in the western SEC is well approximated by the change in oxygen supply associated with the shift in source water composition in the mixture model (simulated ΔO_2 and oxygen supply reconstructed from water mass compositions, $\Delta\text{O}_{2,\text{supply}}$, fall within $\pm 5 \mu\text{mol kg}^{-1}$ of the 1-to-1 line in Fig. 7a). This suggests that changes in remineralization of oxygen might have a relatively low influence compared to changes in transport (Sect. 2.2.3). Furthermore, nearly all of

the changes in oxygen can be accounted for by the changing supply from the Indonesian Throughflow and Southern Pathway (ΔO_2 and $\Delta\text{O}_{2,\text{supply}}$ from Indonesian Throughflow and Southern Pathway Waters alone fall near the 1-to-1 line in 7b). That is, the oxygenation in the western SEC can be accounted for by a shift away from oxygen-poor Indonesian Throughflow Water in favor of oxygen-rich Southern Pathway Water. We note that MPI-ESM1-2-LR is the only ESM in the ensemble which behaves qualitatively differently than the multi-model mean, projecting an increased influence of Indonesian Throughflow Water and weakened influences of Southern Pathway and Arabian Sea Waters in this region (not

shown). MPI-ESM1-2-LR is also the only model that requires significant contributions from remineralization to explain the simulated changes in oxygen. Specifically, the mixture model requires significantly weaker remineralization in the future state than in the historical state to match the simulated oxygen fields (larger oxygenation ΔO_2 than reconstructed from mixture model $\Delta O_{2,\text{supply}}$ for MPI-ESM1-2-LR in Fig. 7a).

The modified water mass composition in the western SEC is then propagated across the Equator by the western boundary current along the Somali coast and then east into the basin interior by the North Equatorial Current, increasing ventilation in the northern basin and accounting for the secondary oxygenation maximum north of the Equator (Fig. 6b). A previous study found that ESMs projected a strengthening of the cross-equatorial transport and North Equatorial Current with warming (Sharma et al., 2023), which may in turn strengthen the northern oxygenation maximum. We note that despite the movement of the $\sigma_0 = 26.4$ surface between the historical and end-of-century states, the results here are not an artifact of this isopycnal displacement (Fig. S14)

3.6 Shoaling marginal sea outflows shift ventilation in the Arabian Sea

We perform a similar analysis as above to assess the role of changing ventilation pathways, namely marginal sea outflows, in the deoxygenation projected in the northern Arabian Sea (Feature 3). Unlike pathways in the southern Indian Ocean, the overall strength of marginal sea outflow transport remains steady under SSP5-8.5 forcing (Fig. S12). Neither the Persian Gulf outflow nor the Red Sea outflow shows any robust trends in volume transport across the ESM ensemble. We hypothesize that, although overall transport from marginal seas does not change, the buoyancy of outflow plumes increases with the rapid heating of marginal seas, which can shoal the outflow plumes and reduce ventilation of the OMZ at thermocline depths. This hypothesis is motivated by the findings of Lachkar et al. (2019), who find that this mechanism can have a strong influence on the OMZ in the Arabian Sea. To test this, we perform a mixture model analysis along the nominal potential density layer $\sigma_0 = 25.7$, which corresponds to the region of deoxygenation in the Arabian Sea (Feature 3; Fig. 8a). We define three source waters for the region: Persian Gulf Water, Red Sea Outflow Water, and Arabian Sea Water (Sect. 2.2.3). We find that the mixture model analysis is able to reconstruct historical and future oxygen, potential temperature, and salinity from the three source water types in the northern Arabian Sea region (see Fig. S15 for a comparison of simulated and reconstructed states in the region of Feature 3).

In the multi-model mean historical state (1950–2015), Persian Gulf Water spreads from the Gulf of Oman across the northern Arabian Sea and Red Sea Water spreads from the Gulf of Aden, while Arabian Sea Water acts as the ambient

water in the basin (Fig. 8b). In the region of Feature 3 (between 60–70° E and 20–25° N), Persian Gulf Water accounts for about 65 % of the water mass in the multi-model mean historical state. Concurrent with the region of deoxygenation in the northern Arabian Sea, there is a decrease in the presence of Persian Gulf Water in the end-of-century mean, which gets replaced by ambient Arabian Sea Water. Averaged over the region of Feature 3, the contribution of Persian Gulf Water decreases to 55 % by the end of the century (decrease in water mass fraction of about 0.1; Fig. 8b). This is also associated with a shift in Persian Gulf Water westward. Further south, there is a decrease in ventilation from Red Sea Outflow Water along $\sigma_0 = 25.7$, which may contribute to deoxygenation off the Omani coast (Fig. 8b).

In five out of the seven ESMs, the simulated deoxygenation in the northern Arabian Sea is well approximated by the change in oxygen supply reconstructed from the shift in water masses in the mixture model (ΔO_2 and $\Delta O_{2,\text{supply}}$ fall within $\pm 5 \mu\text{mol kg}^{-1}$ of the 1-to-1 line in Fig. 9a). We find that the majority of this deoxygenation in the region can be accounted for by changes in oxygen supply by the Persian Gulf (ΔO_2 and $\Delta O_{2,\text{supply}}$ from Persian Gulf Water alone fall close to the 1-to-1 line in Fig. 9b). We note that two ESMs (MPI-ESM1-2-HR and MPI-ESM1-2-LR) exhibit weaker $\Delta O_{2,\text{supply}}$ than ΔO_2 (ESMs fall below the 1-to-1 line in Fig. 9a). While this may suggest that remineralization increases between the historical and future states in these ESMs, this is unlikely given projected changes in export of organic carbon (see next section). Rather, it is likely that the region is poorly described by the source water types given to the mixture model in these two ESMs.

We note that for an alternative analysis where the future state is evaluated at a potential density layer which approximately aligns with the historical depth of $\sigma_0 = 25.7$ (i.e., aliasing from isopycnal displacement is removed; Sect. 2.2.3; Fig. S16), we see greater agreement between the pattern of deoxygenation and decreases in Persian Gulf Water fraction.

3.7 Contributions of biological and stratification changes to oxygen changes

The mixture model analysis suggests that nearly all of the simulated oxygen changes in the western SEC and northern Arabian Sea can be accounted for by shifts in water mass compositions driven by changes in advective ventilation pathways (Figs. 7 and 9). However, the residual oxygen changes that the mixture model analysis does not capture, while small for most ESMs, tend to be systematically biased positive for the western SEC and negative for the northern Arabian Sea. This suggests the influence of additional processes not accounted for in the reconstruction of oxygen supply from the mixture model analysis, in particular the increase in subsurface stratification expected with global warming that can influence the vertical mixing between different water masses, and changes in biological oxygen con-

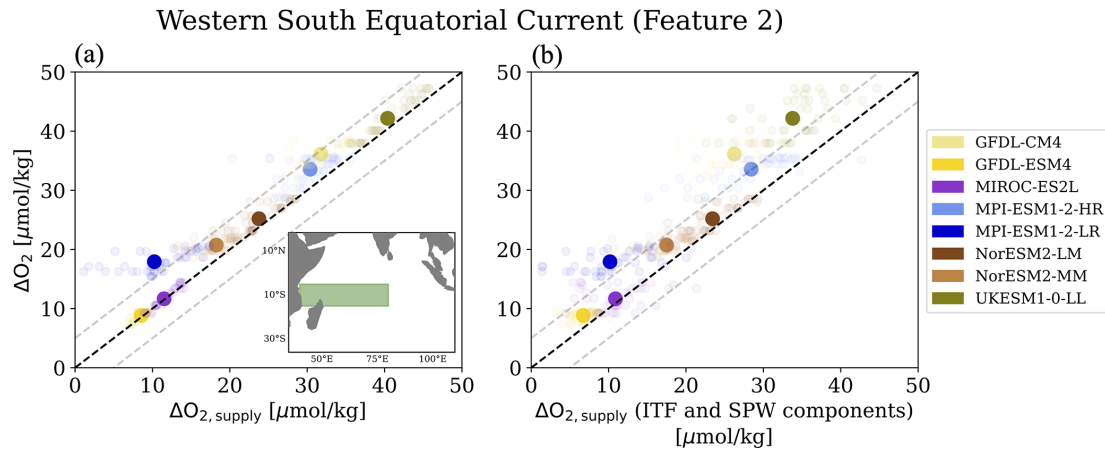


Figure 7. Dissolved oxygen changes computed from water mass composition changes, $\Delta\text{O}_{2,\text{supply}}$, versus total simulated dissolved oxygen changes in the western South Equatorial Current (indicated by the inset in **a**). **(a)** $\Delta\text{O}_{2,\text{supply}}$ from all source water changes. **(b)** $\Delta\text{O}_{2,\text{supply}}$ only from contributions of Indonesian Throughflow and Southern Pathway Waters. Solid markers are means of all samples (faded markers).

sumption along advective pathways once a water parcel has left its source water region.

We examine trends in stratification (for the eight ESMs) and the export of organic carbon at 100 m (available for seven out of eight ESMs) under SSP5-8.5 forcing. The strongest stratification increases are generally confined to the upper 100 m of the water column, but in both the Arabian Sea and SEC regions, the multi-model mean simulates significant stratification increases between 100 and 200 m (about $0.005 \text{ kg m}^{-3} \text{ m}^{-1}$ per century, Fig. 10). These stratification increases are simulated consistently across the ESM ensemble for both regions (Fig. S17). The oxygenation in the SEC region occurs mostly below 200 m, where stratification does not show strong changes, suggesting that changes in vertical mixing likely play a relatively minor role in this region (Fig. 10b and c). In contrast, the deoxygenation in the northern Arabian Sea is largely collocated with the increase in stratification simulated between 100 and 200 m, suggesting that reduced vertical mixing of oxygenated surface waters downward contributes to the deoxygenation projected in this region. Increased subsurface stratification tends to limit the vertical mixing of oxygenated surface waters downward but also limits the mixing of subsurface nutrients into the surface, which in turn limits primary productivity and the export of organic matter at depth and potentially reduces the consumption of oxygen in the subsurface. The export of organic carbon consistently declines under SSP5-8.5 forcing over the Indian Ocean in the multi-model mean, with local maximum declines in the western SEC, the Bay of Bengal, and the Arabian Sea (Figs. 11 and S18 for individual ESMs), suggesting a decline in the consumption of oxygen along ventilation pathways.

The projected decline in export and increase in stratification have opposing effects on oxygen changes and therefore at least partially offset each other. The CMIP6 archive

does not provide the necessary data to quantify the contributions of these two factors to oxygen changes. However, the signs of the residual oxygen changes that remain unexplained by the mixture model analysis can provide some qualitative information on the relative contributions of these two processes. Positive residuals (i.e., stronger oxygenation simulated in ESMs than reconstructed by the mixture model analysis; Fig. 7) suggest that the decline in export dominates over the increase in stratification in the western SEC. In contrast, negative residuals (i.e., stronger deoxygenation simulated in ESMs than reconstructed by the mixture model analysis, Fig. 9) suggest that the influence of increased stratification exceeds the influence of reduced export in the northern Arabian Sea.

4 Discussion

We examine the changes in dissolved oxygen and OMZ volume in response to the high-emissions scenario forcing (SSP5-8.5) in the Indian Ocean using an ensemble of eight CMIP6 Earth system models. In the following, we discuss the three regimes that characterize the OMZ response to warming in the Indian Ocean thermocline (upper 1000 m). We compare this response to that previously investigated for the Pacific Ocean OMZ and to the unstudied response for the Atlantic OMZ, and we contrast the OMZ changes projected in the thermocline with the changes projected in the deep ocean (Fig. 12). We also revise the existing single-pipe and mixing network ventilation framework to interpret the OMZ response of the Indian Ocean, discuss observational constraints on ventilation pathways, and consider caveats in the model ensemble projections.

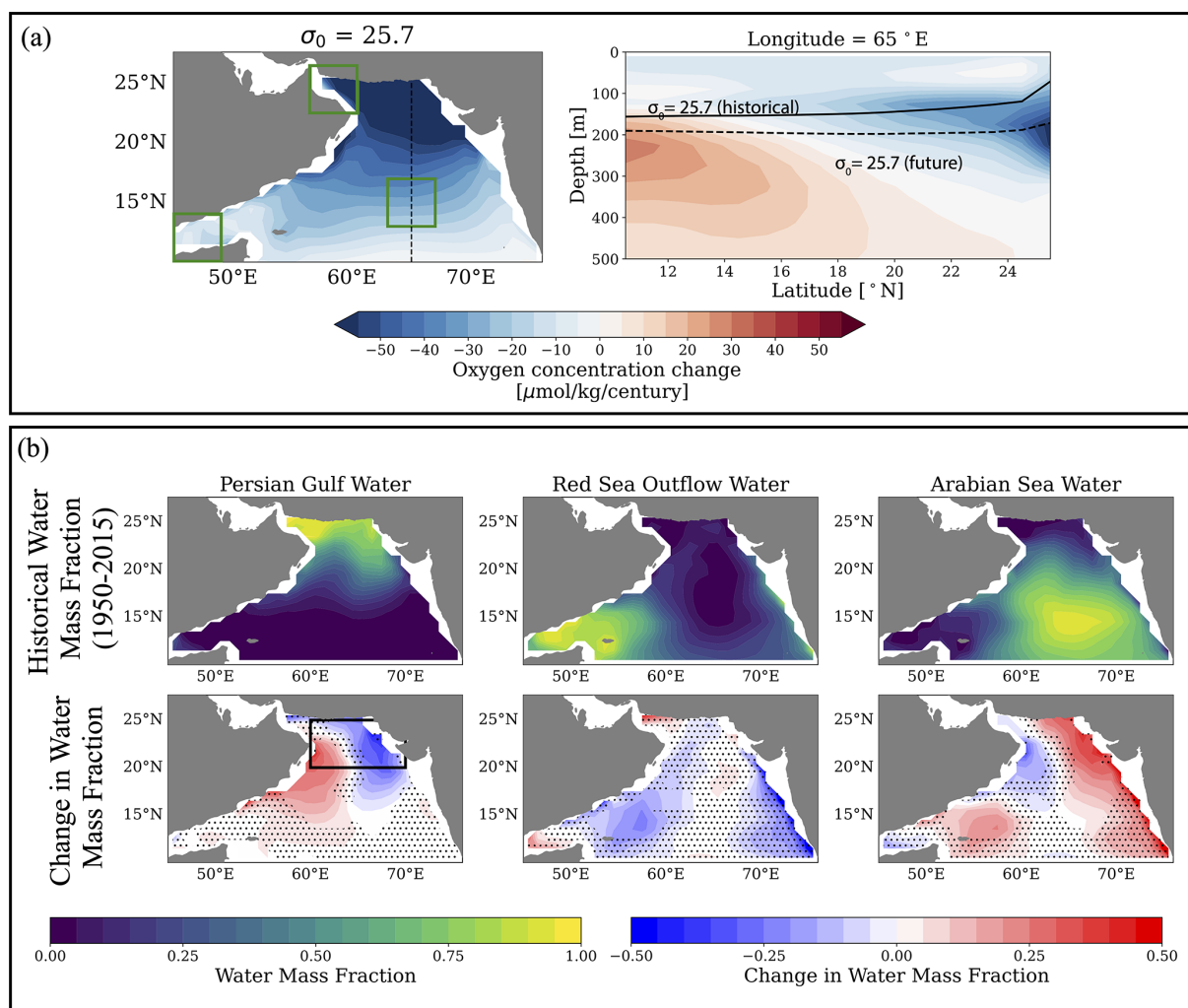


Figure 8. Multi-model mean (MMM) results of mixture model analysis in the Arabian Sea. **(a)** Oxygen changes along the $\sigma_0 = 25.7$ surface and the historical (solid) and end-of-century (dashed) depth of $\sigma_0 = 25.7$ indicated over MMM oxygen changes in depth space at 65°E . Green boxes mark source water regions. **(b)** Historical distribution of Persian Gulf, Red Sea Outflow, and Arabian Sea Water fractions, as well as changes in water mass fractions between historical and end-of-century states. Historical states are calculated as a 1950–2015 mean, and end-of-century states are calculated as a historical mean plus linear trends over 2015–2100. The solid black box in **(b)** shows the region of the northern Arabian Sea over which we report changes. Stippling is shown where less than 75 % (six out of eight) of models agree on the sign of change.

4.1 Three-regime response of the oxygen minimum zone

The response of oxygen and the OMZ in the Indian Ocean thermocline (upper 1000 m) falls into three regimes (Figs. 3a and 12a): a contraction of volume delimited by low oxygen thresholds ($< 85 \mu\text{mol kg}^{-1}$), an expansion of volume delimited by high oxygen thresholds ($> 180 \mu\text{mol kg}^{-1}$), and a redistribution of the volume at intermediate oxygen thresholds (85 to $180 \mu\text{mol kg}^{-1}$). This three-regime response is similar to the OMZ response described in the Pacific Ocean by Busecke et al. (2022) (Fig. 12b). A striking difference between the two basins, however, is the widespread oxygen

gain projected in the Indian Ocean. Indeed, ESMs robustly project an oxygenation of the OMZ cores in the Arabian Sea and Bay of Bengal, similar to the Pacific OMZ core, but also an oxygenation of the southwestern Indian Ocean along the path of the South Equatorial Current and North Equatorial Current. As a result, the OMZ contracts for thresholds as high as $85 \mu\text{mol kg}^{-1}$ (including the volume of hypoxic waters commonly defined by $60 \mu\text{mol kg}^{-1}$) in the Indian Ocean, whereas the contraction is restricted to the very low oxygen levels found in the OMZ core in the Pacific Ocean (typically volume with oxygen less than 10 to $20 \mu\text{mol kg}^{-1}$; Fig. 12a and b). The oxygen gain in the southwestern Indian Ocean is associated with an oxygen loss in the south-

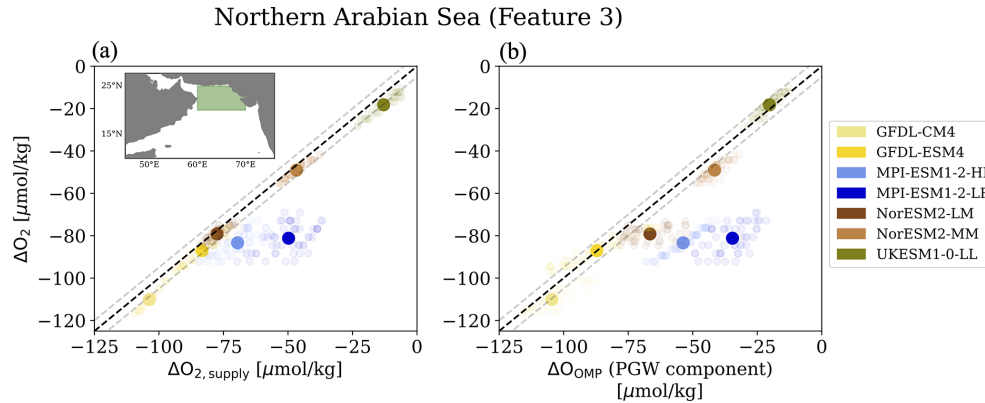


Figure 9. Dissolved oxygen changes computed from water mass composition changes, $\Delta O_{2,\text{supply}}$, versus total simulated dissolved oxygen changes in the northern Arabian Sea (indicated by inset in **a**). **(a)** $\Delta O_{2,\text{supply}}$ from all source water changes. **(b)** $\Delta O_{2,\text{supply}}$ only from contributions of Indonesian Throughflow and Southern Pathway Waters. Solid markers are mean of all samples (faded markers).

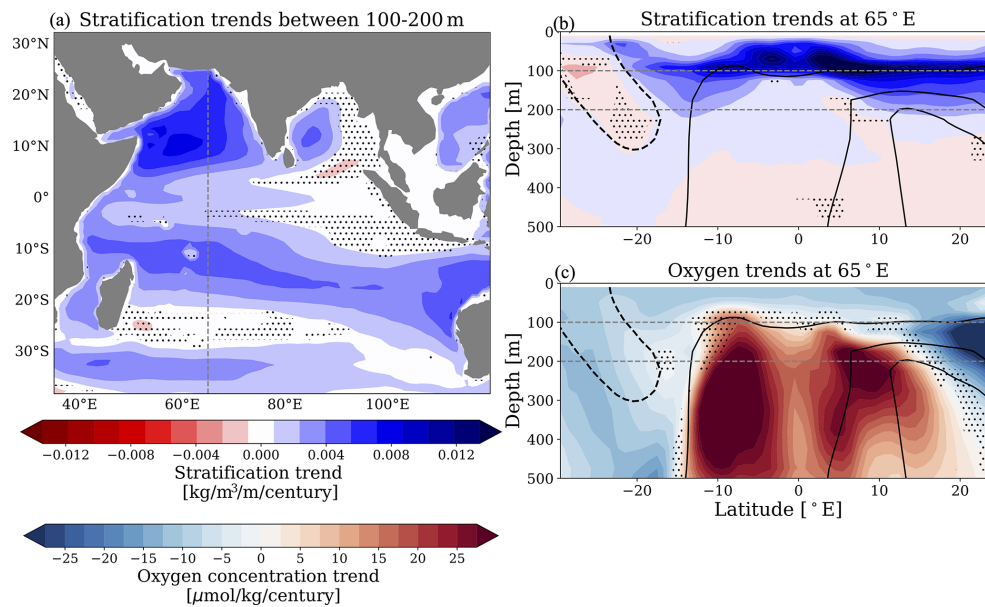


Figure 10. Multi-model mean (MMM) stratification trends under SSP5-8.5 scenario forcing (2015–2100). Stratification trends **(a)** between 100 and 200 m and **(b)** at 65° E. **(c)** Dissolved oxygen trends at 65° E. Dashed gray lines mark **(a)** 65 and 90° E, and panels **(b, c)** show 100 and 200 m. Solid black contours represent 20, 60, and 150 $\mu\text{mol kg}^{-1}$ oxygen. Dashed black contours highlight salinity signatures of Subtropical Underwater (STU). Results are stippled where less than 75% (six out of eight) of models agree on the sign of the trend.

east. This dipole of southwest oxygenation and southeast deoxygenation along the path of the South Equatorial Current explains the redistribution regime and near-zero change in volumes delimited by intermediate oxygen levels (85 to 180 $\mu\text{mol kg}^{-1}$; Fig. 12b). Finally, upstream of the South Equatorial Current, the drastic decline in oxygen supplied by the water masses that enter the thermocline through the south Indian Ocean gyre and Indonesian Throughflow explains the expansion of volumes defined by high oxygen levels (> 180 $\mu\text{mol kg}^{-1}$; Fig. 12a). The slowdown of the Southern Pathway is likely driven by either a weakening of Indian

Central Water or Subantarctic Mode Water formation, but we do not disentangle these two effects in this study.

4.2 Beyond single-pipe and mixing network: cases for two-pipe and moving-pipe systems

The projected oxygenation outside the Indian OMZ core, or shadow zone, calls for a revision of the single-pipe and mixing network ventilation framework used in the Pacific Ocean (Gnanadesikan et al., 2007). In the original framework, increased ventilation and oxygenation with weakened circulation were only reconcilable in shadow zones where there

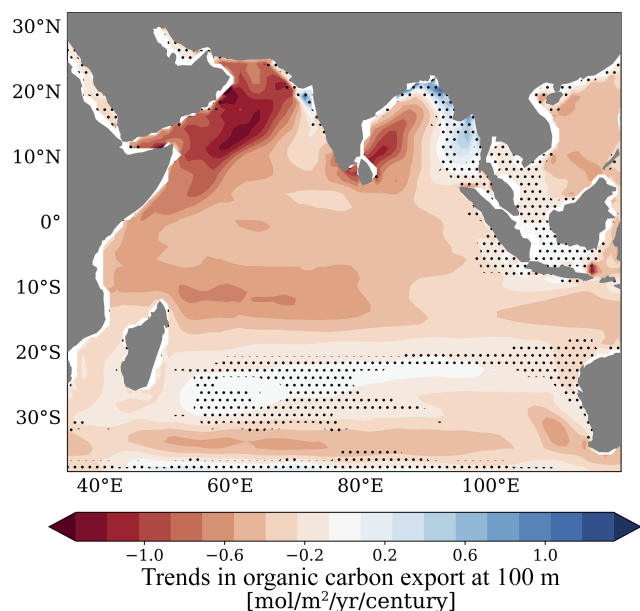


Figure 11. Multi-model mean (MMM) export of organic carbon trends at 100 m under SSP5-8.5 scenario forcing (2015–2100). Results are stippled where less than 75 % (six out of eight) of models agree on the sign of the trend.

are no direct advective ventilation pathways and a mixing network of multiple sources controls ventilation. In both the Pacific and the Indian oceans, the oxygenation of the OMZ core (which is associated with increased ventilation and reduced ideal age) can indeed be interpreted as a shift towards a stronger contribution from younger, oxygen-rich, upper-ocean waters using the mixing network model (Bryan et al., 2006; Gnanadesikan et al., 2007, 2012; Takano et al., 2018; Busecke et al., 2022). In the Pacific, this effect has been attributed to a slowdown of Deep Waters upwelling to thermocline depths, and there is evidence of this same effect in the Indian Ocean basin. In the ESM ensemble used in this study, upwelling of Deep Waters across 1000 m weakens at a rate of 2.0 ± 0.7 Sv per century in the Indian Ocean, even reversing sign to be net downwelling (under SSP5-8.5 forcing in this ESM ensemble, see Fig. S12).

Changes in mixing in the OMZ core, however, are not the primary effect driving oxygenation in the Indian Ocean. In the southern Indian Ocean, ESMs project oxygenation and increased ventilation well outside the shadow zone, within regions of strong advection such as the South Equatorial Current. We show that this oxygenation can be interpreted as a two-pipe system, an intermediate case between a single pipe and a mixing network. Two sources with different oxygen levels, rather than a network of many sources, are in fact sufficient to have increased oxygenation, even though the transport by both ventilation sources weakens. The unique configuration of the Indonesian Throughflow and Southern Pathway merging into the South Equatorial Current allows

for this phenomenon despite intense advection. The ventilation by the Southern Pathway and Indonesian Throughflow declines in response to warming in the ESM ensemble, but the ventilation by the Indonesian Throughflow declines more strongly, favoring the relative contribution of the better-oxygenated Southern Pathway Waters.

Another feature of the Indian Ocean OMZ response which differs from its Pacific Ocean counterpart is the importance of ventilation by marginal sea outflows. We find that changes in ventilation from marginal sea outflows may be a significant driver of deoxygenation in the Arabian Sea. The Persian Gulf rapidly warms in response to global warming, increasing stratification and the buoyancy of outflow water from the Persian Gulf. As outflow water shoals, it becomes unable to ventilate the OMZ in the Arabian Sea and is instead confined to the upper 100 m where its impact on oxygen becomes marginal (the upper ocean is already well oxygenated; Lachkar et al., 2021). The deeper Red Sea outflow plume also shows evidence of shoaling in the ESM ensemble, but it has a weaker impact on the ventilation of the OMZ because its oxygen content is lower than that of the Persian Gulf (on average about $70 \mu\text{mol kg}^{-1}$ for Red Sea Outflow Water versus about $200 \mu\text{mol kg}^{-1}$ for Persian Gulf Water). We can describe this change in the ventilation from marginal seas as a moving pipe, where oxygen supply may be affected by a displacement of a pathway even if the strength of transport along that pathway holds steady.

4.3 Global trends in tropical oxygen minimum zones

Now extending our scope to all tropical oceans, we find that the three-regime OMZ response identified in the Indian (this study) and Pacific (Busecke et al., 2022) oceans is also simulated in the Atlantic Ocean (Figs. 12c and S19). The dynamics driving this three-regime response in the Atlantic have not yet been explored in detail, but it is likely that the even more prominent contraction regime found for the Atlantic OMZ is connected to changes in ventilation by the Atlantic meridional overturning circulation, which is projected to weaken in ESMs (IPCC, 2013; Bakker et al., 2016). This would lead to a favoring of midlatitude waters from the south, as South Atlantic Mode and Intermediate Water subduction rates are projected to hold steady and ventilate lighter densities (Goes et al., 2008; Downes et al., 2009). Looking beyond OMZ volume changes in the ocean thermocline (above 1000 m) to the deep-ocean response (below 1000 m), we see that deoxygenation and OMZ expansion in the deep ocean are more ubiquitous than in the thermocline (Fig. 12d–f). Deoxygenation in the deep ocean is likely due to a slowdown of Deep Water transports as the global thermohaline circulation weakens with warming (e.g., Bakker et al., 2016). When integrating the thermocline and deep-ocean components of the OMZ response to consider the full depth of the water column (similar to what was done for the Pacific Ocean in Busecke et al., 2022), we find that the thermocline response

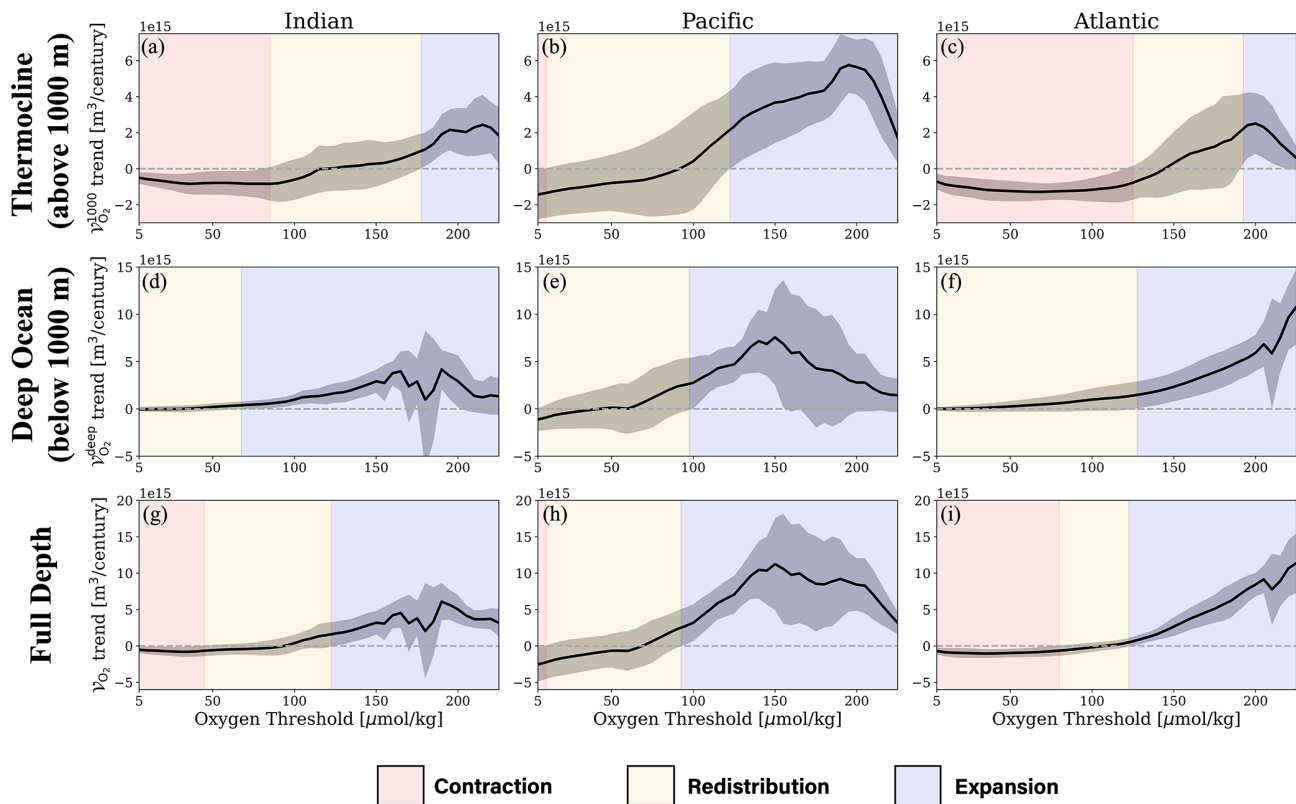


Figure 12. Multi-model mean thermocline OMZ volume trends (above 1000 m) under SSP5-8.5 scenario forcing (2015–2100) as a function of oxygen threshold for the tropical (30° S–30° N) (a) Indian, (b) Pacific, and (c) Atlantic oceans. Deep-ocean (below 1000 m) OMZ volume trends for the tropical (d) Indian, (e) Pacific, and (f) Atlantic oceans. Full-depth OMZ volume trends for the tropical (g) Indian, (h) Pacific, and (i) Atlantic oceans. Shading represents 1 standard deviation of model spread from the mean. Panel (a) is the same as Fig. 3a.

dominates the OMZ contraction at low oxygen thresholds, while the deep-ocean response dominates the expansion at high thresholds (Fig. 12g–i).

4.4 Observational constraints, limitations, and caveats

Projected oxygen changes and thus OMZ volume changes are subject to uncertainties, in particular the magnitude of the oxygenation–deoxygenation dipole along the South Equatorial Current and the deoxygenation in the northern Arabian Sea. The slowdown of the Southern Pathway and Indonesian Throughflow transports is a robust and well-studied feature of ESM projections (Downes et al., 2009; Sen Gupta et al., 2016; Feng et al., 2017; Stellema et al., 2019). The pattern of multi-model mean oxygen trends (Fig. 4) is not sensitive to our model selection protocol, as the three features are also simulated by the six ESMs excluded from the ensemble (Fig. S8). However, when all 14 available ESMs are included in the multi-model mean, we find that the deoxygenation in Features 1 and 3 are enhanced, while the oxygenation in Feature 3 is weakened (Fig. S9).

Historical observations support the slowdown and deoxygenation of the Southern Pathway (Helm et al., 2011;

Kobayashi et al., 2012; Ito et al., 2017; McMonigal et al., 2022). A secular weakening of the Indonesian Throughflow has not yet been observed, possibly obscured by significant decadal variability (Liu et al., 2015; Feng et al., 2018), but there is evidence of forced trends in the global thermohaline circulation that controls the Indonesian Throughflow transport (Rahmstorf et al., 2015; Sun and Thompson, 2020) to support the decline in ventilation by this pathway. However, the relative changes in the two pathways, which control the oxygenation–deoxygenation dipole, are highly uncertain and unconstrained by observations. This dipole pattern has not emerged in current observation-based estimates of historical oxygen trends (Helm et al., 2011; Ito et al., 2017; Schmidtke et al., 2017), though there is some signal of oxygenation near Madagascar in the product of Ito et al. (2017). A detailed study on the time of emergence of oxygen and volume trends identified in this work would require greater availability of large ensembles with biogeochemistry in future generations of CMIP.

Deoxygenation in the northern Arabian Sea has been detected in observations (reviewed by Lachkar et al., 2023). The rapid heating of marginal seas compared to the open ocean and the subsequent increase in stratification and buoy-

ancy of the marginal sea outflows, particularly for the Persian Gulf, are also supported by observations (Al-Yamani et al., 2017; Naqvi, 2021). The projected changes in outflow ventilation are consistent with the findings of ocean model simulation studies, which showed that the warming and shoaling of the Persian Gulf were a major driver of the deoxygenation in the northern Arabian Sea (Lachkar et al., 2019, 2021). Yet, ESMs tend to overestimate the oxygen transport by these marginal sea outflows to the Arabian Sea (e.g., Schmidt et al., 2021 for CMIP5). This partially explains the systematic high oxygen bias in the Arabian Sea in the ensemble of eight CMIP6 ESMs used in this study (Fig. 1) and the absence of suboxia in the five ESMs that were excluded from the ensemble (Table S1), and it could influence the magnitude of the projected deoxygenation associated with the vertical displacement of these outflows. In fact, a study by Vallivatthillam et al. (2023), which applies downscaling methods to CMIP5 projections of Arabian Sea oxygen under high-emission RCP8.5 forcing, finds that the deoxygenation simulated in CMIP5 models in the region is not preserved after the bias-corrected downscaling method is applied (averaging between 200 and 700 m). This suggests that ESM-simulated mean state biases in the Arabian Sea can have a profound impact on the projected changes.

An additional challenge of the mixture model analysis is to distinguish between changes due to source water types and changes in mixing with surface waters. Specifically in the Arabian Sea, Persian Gulf Water and Arabian Sea surface water both tend to be anomalously warm, saline, and well oxygenated. Thus, it is possible that increased stratification and weakened vertical exchange with the surface are interpreted as a decrease in Persian Gulf Water fraction in the mixture model. The presence of northern Arabian Sea deoxygenation in MIROC-ES2L, an ESM which does not resolve the marginal seas and was thus excluded from the OMP analysis for the region, also suggests that stratification increases may play a first-order role in northern Arabian Sea deoxygenation in the ESM ensemble. This is also consistent with a previous study by Lachkar et al. (2021), which investigates deoxygenation in the Arabian Sea from 1982 to 2010 using a high-resolution regional ocean model and attributes about 75 % of ventilation decreases over this period to vertical mixing changes and only 25 % to advective changes. We note that the compensation between the effects of export and stratification changes may in fact be key to allowing the mixture model to perform well in this region.

Further work, including, for example, a full oxygen budget analysis or Lagrangian particle tracking, would be required to better disentangle the effects of marginal sea shoaling and increased stratification in the projections of Arabian Sea oxygen for the ESMs used in this study; however, data for such a study are not currently available. Based on these considerations, the relative effects of marginal sea shoaling and increased stratification in ESM projections of the northern Arabian Sea remain largely uncertain. Ultimately though, the

present study supports the conclusions of the recent review by Lachkar et al. (2023): the Arabian Sea OMZ will be reshaped by changes in stratification and the Persian Gulf outflow driving deoxygenation in the northern subsurface layer, while increased ventilation from the south drives oxygenation of the deeper layers.

5 Conclusion

Oxygen minimum zones can be viewed as multiple concentric layers, like onions, with oxygen concentrations decreasing towards their core. Their response to deoxygenation and global warming in Earth system models falls into three regimes which are controlled by the mechanisms that ventilate these different layers: the outer layers of the oxygen minimum zone expand, the inner layers contract, and in between oxygen is redistributed, leading to near-zero changes in volume but reshaping the spatial distribution of the intermediate layers. We show that this contrast between inner-layer oxygenation and outer-layer deoxygenation, which was first identified in the Pacific Ocean (e.g., Gnanadesikan et al., 2007; Busecke et al., 2022), applies to all tropical oxygen minimum zones. However, the unique geometry and ventilation pathways of the tropical Indian Ocean (bounded by continent to the north, Indonesian Throughflow, and marginal seas) determine what layers of the oxygen minimum zone experience contraction, redistribution, and expansion. The Indian Ocean is characterized by a prominent oxygenation, attributed to changes in the ventilation by the Indonesian Throughflow, and consequently contraction and redistribution regimes that extend to a much larger range of oxygen minimum zone layers than its Pacific counterpart. Furthermore, the rapid warming and shoaling of marginal sea outflows lead to localized deoxygenation in the inner layers of the oxygen minimum zone of the northern Arabian Sea. We identify the response of the Atlantic oxygen minimum zone as also exhibiting regimes of contraction, redistribution, and expansion, but further investigations are required to understand the regional dynamics which produce a pronounced contraction response in that basin.

Appendix A: Mixture model and extended optimum multiparameter analysis

The mixture model used in this study is based on extended optimum multiparameter (OMP) analysis (OMP; Karstensen and Tomczak, 1998), which is a method of solving an overdetermined linear mixture model that takes into account the conversion of one tracer to another, generally by remineralization. Detailed explanations of the OMP method can be found in Tomczak and Large (1989) and Shrikumar et al. (2022), but here we give a brief summary.

First, we define a set of N source water types with properties, p . Let e_p^i be the values for property p and i th source

water mass. Each sample in the evaluation region has a value for each property, s_p^j . The goal is to solve for the fraction of i th source water type in each sample, x_i^j . We can define the objective function:

$$\sum_{i=1}^N e_p^i x_i^j = s_p^j + \epsilon_p^j, \quad (\text{A1})$$

where ϵ_p^j is a residual to minimize. Using user-defined weights, W , to assign relative importance to each property, the residual takes the form

$$\epsilon_p^j = W_p \left(\sum_i (e_p^i - \mu_p) x_i^j + r_B^A \Delta_j^B - (s_p^j - \mu_p) \right), \quad (\text{A2})$$

where we center the values for each property, e_p^i with their mean, μ_p . The user-defined weights play the role of normalizing across fields. We chose to set the weight for dissolved oxygen and AOU at 2% of the weight of potential temperature and salinity fields to account for the greater range of values in sources of dissolved oxygen. The results of the analysis are not sensitive to small changes in weight values. The term $r_B^A \Delta_j^B$ allows for the conservation of two properties, A and B , which are exchanged via remineralization. The cost function is thus defined as the sum of residuals for every property, p , as well as a mass conservation term ϵ_M^j which penalizes deviations from total mass fractions of unity for each sample point.

$$C^j = (\epsilon_M^j)^2 + \sum_p (\epsilon_p^j)^2 \quad (\text{A3})$$

The pyOMPA implementation of this method allows for a hard constraint on mass conservation rather than minimizing a residual (Shrikumar et al., 2022). However, we do not use this feature and thus recover the original method of Karstensen and Tomczak (1998).

We note that the mixing model used in this study differs in several ways from the traditional extended OMP. We solve a “mixing triangle” of three source water types rather than four as used in, for example, Tomczak (1981). Adding an extra degree of freedom to track remineralization, we thus have a total of 4 degrees of freedom. Typically, remineralization is tracked as the conversion of oxygen to phosphate and nitrate using Redfield ratios. Since we do not have access to full nutrient fields for the ESM experiments used in this study, we simply allow for the conversion of oxygen to AOU with a ratio of -1 . As constraints, we use potential temperature, salinity, dissolved oxygen, AOU, and mass conservation. Since AOU is a function of dissolved oxygen, potential temperature, and salinity, we have four unique constraints. Thus, our mixture model is equivalent to a determined set of linear equations rather than an overdetermined set (i.e., “multiparameter analysis” rather than “optimum multiparameter analysis”; Tomczak, 1981; Tomczak and Large, 1989). However, since AOU must also be included in the calculation, we

leverage the least-squares method used in solving the overdetermined problem.

Code and data availability. The processed data files and code to reproduce results presented here are available at <https://doi.org/10.5281/zenodo.8342233> (Ditkovsky, 2023).

Supplement. The supplement related to this article is available online at: <https://doi.org/10.5194/bg-20-4711-2023-supplement>.

Author contributions. Conceptualization: SD, LR, JB. Data curation: SD, JB. Formal analysis: SD. Funding acquisition: LR. Investigation: SD, LR. Methodology: SD, LR, JB. Software: SD, JB. Supervision: LR. Visualization: SD. Writing – original draft: SD, LR. Writing – review and editing: SD, LR, JB.

Competing interests. The contact author has declared that none of the authors has any competing interests.

Disclaimer. Publisher’s note: Copernicus Publications remains neutral with regard to jurisdictional claims made in the text, published maps, institutional affiliations, or any other geographical representation in this paper. While Copernicus Publications makes every effort to include appropriate place names, the final responsibility lies with the authors.

Special issue statement. This article is part of the special issue “Low-oxygen environments and deoxygenation in open and coastal marine waters”. It is a result of the 53rd International Colloquium on Ocean Dynamics (3rd GO2NE Oxygen Conference), Liège, Belgium, 16–20 May 2022.

Acknowledgements. The authors acknowledge the World Climate Research Programme, which, through its Working Group on Coupled Modelling, coordinated and promoted CMIP6, participating climate modeling groups for producing and publishing their model output, the Earth System Grid Federation (ESGF) for archiving the data and providing access, and the multiple funding agencies who support CMIP6 and ESGF. The authors further thank David Luet for his technical support and his help in creating a mirrored subset of the CMIP6 archive on the Princeton HPC, which was used for the final analysis. The authors thank Jasmin G. John and John P. Dunne at GFDL for providing additional Earth system model data not available via ESGF.

Financial support. Sam Ditkovsky and Laure Resplandy have been supported by NSF CAREER under award no. 2042672 and the Princeton University High Meadows Environmental Institute Grand Challenge Award for this study. Julius Busecke has been supported by the Gordon and Betty Moore Foundation (grant 8434).

Review statement. This paper was edited by Marilaure Grégoire and reviewed by Anand Gnanadesikan, Zouhair Lachkar, and one anonymous referee.

References

- Abernathy, R. P., Busecke, J. J. M., Smith, T. A., Deauna, J. D., Banihirwe, A., Nicholas, T., Fernandes, F., James, B., Dussin, R., Cherian, D. A., Caneill, R., Sinha, A., Uieda, L., Rath, W., Balwada, D., Constantinou, N. C., Ponte, A., Zhou, Y., Uchida, T., and Thielen, J.: xgcm, Zenodo [code], <https://doi.org/10.5281/zenodo.7348619>, 2022.
- Al Azhar, M., Lachkar, Z., Lévy, M., and Smith, S.: Oxygen minimum zone contrasts between the Arabian Sea and the Bay of Bengal implied by differences in remineralization depth, *Geophys. Res. Lett.*, 44, 11–106, 2017.
- Al-Yamani, F., Yamamoto, T., Al-Said, T., and Alghunaim, A.: Dynamic hydrographic variations in northwestern Arabian Gulf over the past three decades: Temporal shifts and trends derived from long-term monitoring data, *Mar. Pollut. Bull.*, 122, 488–499, 2017.
- Auderset, A., Moretti, S., Taphorn, B., Ebner, P.-R., Kast, E., Wang, X. T., Schiebel, R., Sigman, D. M., Haug, G. H., and Martínez-García, A.: Enhanced ocean oxygenation during Cenozoic warm periods, *Nature*, 609, 77–82, 2022.
- Bakker, P., Schmittner, A., Lenaerts, J., Abe-Ouchi, A., Bi, D., van den Broeke, M., Chan, W.-L., Hu, A., Beadling, R., Marsland, S., and Mernild, S. H.: Fate of the Atlantic Meridional Overturning Circulation: Strong decline under continued warming and Greenland melting, *Geophys. Res. Lett.*, 43, 12–252, 2016.
- Banse, K., Naqvi, S. W. A., Narvekar, P. V., Postel, J. R., and Jayakumar, D. A.: Oxygen minimum zone of the open Arabian Sea: variability of oxygen and nitrite from daily to decadal timescales, *Biogeosciences*, 11, 2237–2261, <https://doi.org/10.5194/bg-11-2237-2014>, 2014.
- Beal, L. M., Ffield, A., and Gordon, A. L.: Spreading of Red Sea overflow waters in the Indian Ocean, *J. Geophys. Res.-Oceans*, 105, 8549–8564, 2000.
- Bentsen, M., Olivieri, D. J. L., Seland, Y., Toniazzo, T., Gjermundsen, A., Graff, L. S., Debernard, J. B., Gupta, A. K., He, Y., Kirkevåg, A., Schwinger, J., Tjiputra, J., Aas, K. S., Bethke, I., Fan, Y., Griesfeller, J., Grini, A., Guo, C., Ilicak, M., Karset, I. H. H., Landgren, O. A., Liakka, J., Moseid, K. O., Nummelin, A., Spensberger, C., Tang, H., Zhang, Z., Heinze, C., Iversen, T., and Schulz, M.: NCC NorESM2-MM model output prepared for CMIP6 CMIP, World Climate Research Programme (WCRP) [data set], <https://doi.org/10.22033/ESGF/CMIP6.506>, 2019a.
- Bentsen, M., Olivieri, D. J. L., Seland, Y., Toniazzo, T., Gjermundsen, A., Graff, L. S., Debernard, J. B., Gupta, A. K., He, Y., Kirkevåg, A., Schwinger, J., Tjiputra, J., Aas, K. S., Bethke, I., Fan, Y., Griesfeller, J., Grini, A., Guo, C., Ilicak, M., Karset, I. H. H., Landgren, O. A., Liakka, J., Moseid, K. O., Nummelin, A., Spensberger, C., Tang, H., Zhang, Z., Heinze, C., Iversen, T., and Schulz, M.: NCC NorESM2-MM model output prepared for CMIP6 ScenarioMIP, World Climate Research Programme (WCRP) [data set], <https://doi.org/10.22033/ESGF/CMIP6.608>, 2019b.
- Bertrand, A., Chaigneau, A., Peraltilla, S., Ledesma, J., Graco, M., Monetti, F., and Chavez, F. P.: Oxygen: a fundamental property regulating pelagic ecosystem structure in the coastal southeastern tropical Pacific, *PLoS one*, 6, e29558, <https://doi.org/10.1371/journal.pone.0029558>, 2011.
- Bindoff, N. L., Cheung, W. W., Kairo, J. G., Arístegui, J., Guinder, V. A., Hallberg, R., Hilmi, N. J. M., Jiao, N., Karim, M. S., Levin, L., O'Donoghue, S., Purca, S. R., Tagliabue, A., Rinkevich, B., Suga, T., Tagliabue, A., and Williamson, P.: Changing Ocean, Marine Ecosystems, and Dependent Communities, in: IPCC Special Report on the Ocean and Cryosphere in a Changing Climate, edited by: Portner, H.-O., Roberts, D. C., Masson-Delmotte, V., Zhai, P., Tignor, M., Poloczanska, E., Mintenbeck, K., Alegria, A., Nicolai, M., Okem, A., Petzold, J., Rama, B., and Weyer, N. M., Cambridge University Press, Cambridge, UK and New York, NY, USA, 447–587, <https://doi.org/10.1017/9781009157964.007>, 2019.
- Bopp, L., Resplandy, L., Orr, J. C., Doney, S. C., Dunne, J. P., Gehlen, M., Halloran, P., Heinze, C., Ilyina, T., Séférian, R., Tjiputra, J., and Vichi, M.: Multiple stressors of ocean ecosystems in the 21st century: projections with CMIP5 models, *Biogeosciences*, 10, 6225–6245, <https://doi.org/10.5194/bg-10-6225-2013>, 2013.
- Bopp, L., Resplandy, L., Untersee, A., Le Mezo, P., and Kageyama, M.: Ocean (de) oxygenation from the Last Glacial Maximum to the twenty-first century: insights from Earth System models, *Philos. T. Roy. Soc. A*, 375, 20160323, <https://doi.org/10.1098/rsta.2016.0323>, 2017.
- Bouchard, C. and Crumplin, W.: Neglected no longer: the Indian Ocean at the forefront of world geopolitics and global geostrategy, *Journal of the Indian Ocean Region*, 6, 26–51, 2010.
- Brandt, P., Bange, H. W., Banyte, D., Dengler, M., Didwischus, S.-H., Fischer, T., Greatbatch, R. J., Hahn, J., Kanzow, T., Karstensen, J., Körtzinger, A., Krahlmann, G., Schmidtke, S., Stramma, L., Tanhua, T., and Visbeck, M.: On the role of circulation and mixing in the ventilation of oxygen minimum zones with a focus on the eastern tropical North Atlantic, *Biogeosciences*, 12, 489–512, <https://doi.org/10.5194/bg-12-489-2015>, 2015.
- Brill, R. W.: A review of temperature and oxygen tolerance studies of tunas pertinent to fisheries oceanography, movement models and stock assessments, *Fish. Oceanogr.*, 3, 204–216, <https://doi.org/10.1111/j.1365-2419.1994.tb00098.x>, 1994.
- Brill, R. W.: Selective advantages conferred by the high performance physiology of tunas, billfishes, and dolphin fish, *Comp. Biochem. Phys. A*, 113, 3–15, 1996.
- Bryan, F. O., Danabasoglu, G., Gent, P. R., and Lindsay, K.: Changes in ocean ventilation during the 21st century in the CCSM3, *Ocean Model.*, 15, 141–156, 2006.
- Busecke, J. J., Resplandy, L., Ditkovsky, S. J., and John, J. G.: Diverging fates of the Pacific Ocean oxygen minimum zone and its core in a warming world, *AGU Advances*, 3, e2021AV000470, <https://doi.org/10.1029/2021AV000470>, 2022.
- Busecke, J. J. M. and Spring, A.: [jbusecke/cmip6_preprocessing:v0.1.4](https://doi.org/10.5281/zenodo.3743397), Zenodo [code], <https://doi.org/10.5281/zenodo.3743397>, 2020.
- Cabré, A., Marinov, I., Bernardello, R., and Bianchi, D.: Oxygen minimum zones in the tropical Pacific across CMIP5 models: mean state differences and climate change trends, *Biogeosciences*, 20, 4711–4736, 2023

- sciences, 12, 5429–5454, <https://doi.org/10.5194/bg-12-5429-2015>, 2015.
- Christian, J. R., Denman, K. L., Hayashida, H., Holdsworth, A. M., Lee, W. G., Riche, O. G. J., Shao, A. E., Steiner, N., and Swart, N. C.: Ocean biogeochemistry in the Canadian Earth System Model version 5.0.3: CanESM5 and CanESM5-CanOE, *Geosci. Model Dev.*, 15, 4393–4424, <https://doi.org/10.5194/gmd-15-4393-2022>, 2022.
- Clifton, J., Etienne, M., Barnes, D. K., Barnes, R. S., Suggett, D. J., and Smith, D. J.: Marine conservation policy in Seychelles: Current constraints and prospects for improvement, *Mar. Policy*, 36, 823–831, 2012.
- Cocco, V., Joos, F., Steinacher, M., Frölicher, T. L., Bopp, L., Dunne, J., Gehlen, M., Heinze, C., Orr, J., Oschlies, A., Schneider, B., Segschneider, J., and Tjiputra, J.: Oxygen and indicators of stress for marine life in multi-model global warming projections, *Biogeosciences*, 10, 1849–1868, <https://doi.org/10.5194/bg-10-1849-2013>, 2013.
- Deutsch, C., Berelson, W., Thunell, R., Weber, T., Tems, C., McManus, J., Crusius, J., Ito, T., Baumgartner, T., Ferreira, V., Mey, J., and Van Geen, A.: Centennial changes in North Pacific anoxia linked to tropical trade winds, *Science*, 345, 665–668, 2014.
- Deutsch, C., Penn, J. L., and Seibel, B.: Metabolic trait diversity shapes marine biogeography, *Nature*, 585, 557–562, 2020.
- Ditkovsky, S.: Data and software for submission of “Unique ocean circulation pathways reshape the Indian Ocean oxygen minimum zone with warming”, Zenodo [code, data set], <https://doi.org/10.5281/zenodo.8342233>, 2023.
- Downes, S. M., Bindoff, N. L., and Rintoul, S. R.: Impacts of climate change on the subduction of mode and intermediate water masses in the Southern Ocean, *J. Climate*, 22, 3289–3302, 2009.
- Dunne, J. P., Horowitz, L., Adcroft, A., Ginoux, P., Held, I., John, J., Krasting, J. P., Malyshev, S., Naik, V., Paulot, F., Shevliakova, E., Stock, C. A., Zadeh, N., Balaji, V., Blanton, C., Dunne, K. A., Dupuis, C., Durachta, J., Dussin, R., Gauthier, P. P. G., Griffies, S. M., Guo, H., Hallberg, R. W., Harrison, M., He, J., Hurlin, W., McHugh, C., Menzel, R., Milly, P. C. D., Nikonov, S., Paynter, D. J., Ploshay, J., Radhakrishnan, A., Rand, K., Reichl, B. G., Robinson, T., Schwarzkopf, D. M., Sentman, L. T., Underwood, S., Vahlenkamp, H., Winton, M., Wittenberg, A. T., Wyman, B., Zeng, Y., and Zhao, M.: The GFDL Earth System Model version 4.1 (GFDL-ESM 4.1): Overall coupled model description and simulation characteristics, *J. Adv. Model. Earth Sy.*, 12, e2019MS002015, <https://doi.org/10.1029/2019MS002015>, 2020.
- Duteil, O., Böning, C. W., and Oschlies, A.: Variability in subtropical-tropical cells drives oxygen levels in the tropical Pacific Ocean, *Geophys. Res. Lett.*, 41, 8926–8934, 2014.
- Duteil, O., Frenger, I., and Getzlaff, J.: The riddle of eastern tropical Pacific Ocean oxygen levels: the role of the supply by intermediate-depth waters, *Ocean Sci.*, 17, 1489–1507, <https://doi.org/10.5194/os-17-1489-2021>, 2021.
- Eyring, V., Bony, S., Meehl, G. A., Senior, C. A., Stevens, B., Stouffer, R. J., and Taylor, K. E.: Overview of the Coupled Model Intercomparison Project Phase 6 (CMIP6) experimental design and organization, *Geosci. Model Dev.*, 9, 1937–1958, <https://doi.org/10.5194/gmd-9-1937-2016>, 2016.
- Feng, M., Zhang, X., Sloyan, B., and Chamberlain, M.: Contribution of the deep ocean to the centennial changes of the Indonesian Throughflow, *Geophys. Res. Lett.*, 44, 2859–2867, 2017.
- Feng, M., Zhang, N., Liu, Q., and Wijffels, S.: The Indonesian throughflow, its variability and centennial change, *Geoscience Letters*, 5, 1–10, 2018.
- Fine, R. A.: Circulation of Antarctic intermediate water in the South Indian Ocean, *Deep-Sea Res. Pt. I*, 40, 2021–2042, 1993.
- Firing, E., Fernandes, F., Barna, A., and Abernathy, R.: GSW-python: Python implementation of the Thermodynamic Equation of Seawater 2010 (TEOS-10), Zenodo [code], <https://doi.org/10.5281/zenodo.4631363>, 2021.
- Garcia, H., Weathers, K., Paver, C., Smolyar, I., Boyer, T., Locarnini, M., Zweng, M., Mishonov, A., Baranova, O., Seidov, D., and Reagan, J. R.: World Ocean Atlas 2018, Vol. 3: Dissolved Oxygen, Apparent Oxygen Utilization, and Dissolved Oxygen Saturation, Technical editor: Mishonov, A., NOAA, <https://archimer.ifremer.fr/doc/00651/76337/> (last access: 16 November 2023), 2019.
- Gattuso, J.-P., Magnan, A., Billé, R., Cheung, W. W., Howes, E. L., Joos, F., Allemand, D., Bopp, L., Cooley, S. R., Eakin, C. M., Hoegh-Guldberg, O., Kelly, R. P., Pörtner, H.-O., Rogers, A. D., Baxter, J. M., Laffoley, D., Osborn, D., Rankovic, A., Rochette, J., Sumaila, U. R., Treyer, S., and Turley, C.: Contrasting futures for ocean and society from different anthropogenic CO₂ emissions scenarios, *Science*, 349, aac4722, <https://doi.org/10.1126/science.aac4722>, 2015.
- Gnanadesikan, A., Russell, J. L., and Zeng, F.: How does ocean ventilation change under global warming?, *Ocean Sci.*, 3, 43–53, <https://doi.org/10.5194/os-3-43-2007>, 2007.
- Gnanadesikan, A., Dunne, J. P., and John, J.: Understanding why the volume of suboxic waters does not increase over centuries of global warming in an Earth System Model, *Biogeosciences*, 9, 1159–1172, <https://doi.org/10.5194/bg-9-1159-2012>, 2012.
- Gnanadesikan, A., Bianchi, D., and Pradal, M.-A.: Critical role for mesoscale eddy diffusion in supplying oxygen to hypoxic ocean waters, *Geophys. Res. Lett.*, 40, 5194–5198, 2013.
- Goes, M., Wainer, I., Gent, P. R., and Bryan, F. O.: Changes in subduction in the South Atlantic Ocean during the 21st century in the CCSM3, *Geophys. Res. Lett.*, 35, L06701, <https://doi.org/10.1029/2007GL032762>, 2008.
- Good, P., Sellar, A., Tang, Y., Rumbold, S., Ellis, R., Kelley, D., Kuhlbrodt, T., and Walton, J.: MOHC UKESM1.0-LL model output prepared for CMIP6 ScenarioMIP, <https://doi.org/10.22033/ESGF/CMIP6.1567>, 2019.
- Guo, H., John, J. G., Blanton, C., McHugh, C., Nikonov, S., Radhakrishnan, A., Rand, K., Zadeh, N. T., Balaji, V., Durachta, J., Dupuis, C., Menzel, R., Robinson, T., Underwood, S., Vahlenkamp, H., Bushuk, M., Dunne, K. A., Dussin, R., Gauthier, P. P., Ginoux, P., Griffies, S. M., Hallberg, R., Harrison, M., Hurlin, W., Lin, P., Malyshev, S., Naik, V., Paulot, F., Paynter, D. J., Ploshay, J., Reichl, B. G., Schwarzkopf, D. M., Seman, C. J., Shao, A., Silvers, L., Wyman, B., Yan, X., Zeng, Y., Adcroft, A., Dunne, J. P., Held, I. M., Krasting, J. P., Horowitz, L. W., Milly, P., Shevliakova, E., Winton, M., Zhao, M., and Zhang, R.: NOAA-GFDL GFDL-CM4 model output, World Climate Research Programme (WCRP) [data set], <https://doi.org/10.22033/ESGF/CMIP6.1402>, 2018a.

- Guo, H., John, J. G., Blanton, C., McHugh, C., Nikonov, S., Radhakrishnan, A., Rand, K., Zadeh, N. T., Balaji, V., Durachta, J., Dupuis, C., Menzel, R., Robinson, T., Underwood, S., Vahlenkamp, H., Dunne, K. A., Gauthier, P. P., Ginoux, P., Griffies, S. M., Hallberg, R., Harrison, M., Hurlin, W., Lin, P., Malyshev, S., Naik, V., Paulot, F., Paynter, D. J., Ploshay, J., Schwarzkopf, D. M., Seman, C. J., Shao, A., Silvers, L., Wyman, B., Yan, X., Zeng, Y., Adcroft, A., Dunne, J. P., Held, I. M., Krasting, J. P., Horowitz, L. W., Milly, C., Shevliakova, E., Winton, M., Zhao, M., and Zhang, R.: NOAA-GFDL GFDL-CM4 model output prepared for CMIP6 ScenarioMIP, World Climate Research Programme (WCRP) [data set], <https://doi.org/10.22033/ESGF/CMIP6.9242>, 2018b.
- Hajima, T., Abe, M., Arakawa, O., Suzuki, T., Komuro, Y., Ogura, T., Ogochi, K., Watanabe, M., Yamamoto, A., Tatebe, H., Noguchi, M. A., Ohgaito, R., Ito, A., Yamazaki, D., Ito, A., Takata, K., Watanabe, S., Kawamiya, M., and Tachiiri, K.: MIROC MIROC-ES2L model output prepared for CMIP6 CMIP, World Climate Research Programme (WCRP) [data set], <https://doi.org/10.22033/ESGF/CMIP6.902>, 2019.
- Harper, S.: Thermocline ventilation and pathways of tropical–subtropical water mass exchange, *Tellus A*, 52, 330–345, 2000.
- Held, I., Guo, H., Adcroft, A., Dunne, J., Horowitz, L., Krasting, J., Shevliakova, E., Winton, M., Zhao, M., Bushuk, M., Wittenberg, A. T., Wyman, B., Xiang, B., Zhang, R., Anderson, W., Balaji, V., Donner, L., Dunne, K., Durachta, J., Gauthier, P. P. G., Ginoux, P., Golaz, J.-C., Griffies, S. M., Hallberg, R., Harris, L., Harrison, M., Hurlin, W., John, J., Lin, P., Lin, S.-J., Malyshev, S., Menzel, R., Milly, P. C. D., Ming, Y., Naik, V., Paynter, D., Paulot, F., Ramaswamy, V., Reichl, B., Robinson, T., Rosati, A., Seman, C., Silvers, L. G., Underwood, S., and Zadeh, N.: Structure and performance of GFDL’s CM4.0 climate model, *J. Adv. Model. Earth Sy.*, 11, 3691–3727, 2019.
- Helm, K. P., Bindoff, N. L., and Church, J. A.: Observed decreases in oxygen content of the global ocean, *Geophys. Res. Lett.*, 38, L23602, <https://doi.org/10.1029/2011GL049513>, 2011.
- IPCC: Climate change 2013: the physical science basis, Contribution of Working Group I to the Fifth Assessment Report of the Intergovernmental Panel on Climate Change, edited by: Stocker, T. F., Qin, D., Plattner, G. K., Tignor, M., Allen, S. K., Boschung, J., Nauels, A., Xia, Y., Bex, V., and Midgley, P. M., Cambridge University Press, Cambridge, UK and New York, NY, USA, ISBN 978-1-107-05799-9, 2013.
- Ito, T., Minobe, S., Long, M. C., and Deutsch, C.: Upper ocean O₂ trends: 1958–2015, *Geophys. Res. Lett.*, 44, 4214–4223, 2017.
- John, J. G., Blanton, C., McHugh, C., Radhakrishnan, A., Rand, K., Vahlenkamp, H., Wilson, C., Zadeh, N. T., Dunne, J. P., Dussin, R., Horowitz, L. W., Krasting, J. P., Lin, P., Malyshev, S., Naik, V., Ploshay, J., Shevliakova, E., Silvers, L., Stock, C., Winton, M., and Zeng, Y.: NOAA-GFDL GFDL-ESM4 model output prepared for CMIP6 ScenarioMIP, World Climate Research Programme (WCRP) [data set], <https://doi.org/10.22033/ESGF/CMIP6.1414>, 2018.
- Jungclauss, J., Bittner, M., Wieners, K.-H., Wachsmann, F., Schupfner, M., Legutke, S., Giorgetta, M., Reick, C., Gayler, V., Haak, H., de Vrese, P., Raddatz, T., Esch, M., Mauritsen, T., von Storch, J.-S., Behrens, J., Brovkin, V., Claussen, M., Crueger, T., Fast, I., Fiedler, S., Hagemann, S., Hohenegger, C., Jahns, T., Kloster, S., Kinne, S., Lasslop, G., Kornbluh, L., Marotzke, J., Matei, D., Meraner, K., Mikolajewicz, U., Modali, K., Müller, W., Nabel, J., Notz, D., Peters, K., Pincus, R., Pohlmann, H., Pongratz, J., Rast, S., Schmidt, H., Schnur, R., Schulzweida, U., Six, K., Stevens, B., Voigt, A., and Roeckner, E.: MPI-M MPIESM1.2-HR model output prepared for CMIP6 CMIP, World Climate Research Programme (WCRP) [data set], <https://doi.org/10.22033/ESGF/CMIP6.741>, 2019.
- Karstensen, J. and Quadfasel, D.: Water subducted into the Indian Ocean subtropical gyre, *Deep-Sea Res. Pt. II*, 49, 1441–1457, 2002.
- Karstensen, J. and Tomczak, M.: Ventilation processes and water mass ages in the thermocline of the southeast Indian Ocean, *Geophys. Res. Lett.*, 24, 2777–2780, 1997.
- Karstensen, J. and Tomczak, M.: Age determination of mixed water masses using CFC and oxygen data, *J. Geophys. Res.-Oceans*, 103, 18599–18609, 1998.
- Keeling, R. F., Körtzinger, A., and Gruber, N.: Ocean deoxygenation in a warming world, *Annu. Rev. Mar. Sci.*, 2, 199–229, 2010.
- Kobayashi, T., Mizuno, K., and Suga, T.: Long-term variations of surface and intermediate waters in the southern Indian Ocean along 32 S, *J. Oceanogr.*, 68, 243–265, 2012.
- Krasting, J. P., John, J. G., Blanton, C., McHugh, C., Nikonov, S., Radhakrishnan, A., Rand, K., Zadeh, N. T., Balaji, V., Durachta, J., Dupuis, C., Menzel, R., Robinson, T., Underwood, S., Vahlenkamp, H., Dunne, K. A., Gauthier, P. P., Ginoux, P., Griffies, S. M., Hallberg, R., Harrison, M., Hurlin, W., Malyshev, S., Naik, V., Paulot, F., Paynter, D. J., Ploshay, J., Reichl, B. G., Schwarzkopf, D. M., Seman, C. J., Silvers, L., Wyman, B., Zeng, Y., Adcroft, A., Dunne, J. P., Dussin, R., Guo, H., He, J., Held, I. M., Horowitz, L. W., Lin, P., Milly, P., Shevliakova, E., Stock, C., Winton, M., Wittenberg, A. T., Xie, Y., and Zhao, M.: NOAA-GFDL GFDL-ESM4 model output prepared for CMIP6 CMIP, World Climate Research Programme (WCRP) [data set], <https://doi.org/10.22033/ESGF/CMIP6.1407>, 2018.
- Kwiatkowski, L., Torres, O., Bopp, L., Aumont, O., Chamberlain, M., Christian, J. R., Dunne, J. P., Gehlen, M., Ilyina, T., John, J. G., Lenton, A., Li, H., Lovenduski, N. S., Orr, J. C., Palmieri, J., Santana-Falcón, Y., Schwinger, J., Séférian, R., Stock, C. A., Tagliabue, A., Takano, Y., Tjiputra, J., Toyama, K., Tsujino, H., Watanabe, M., Yamamoto, A., Yool, A., and Ziehn, T.: Twenty-first century ocean warming, acidification, deoxygenation, and upper-ocean nutrient and primary production decline from CMIP6 model projections, *Biogeosciences*, 17, 3439–3470, <https://doi.org/10.5194/bg-17-3439-2020>, 2020.
- Lachkar, Z., Smith, S., Lévy, M., and Pauluis, O.: Eddies reduce denitrification and compress habitats in the Arabian Sea, *Geophys. Res. Lett.*, 43, 9148–9156, 2016.
- Lachkar, Z., Lévy, M., and Smith, K. S.: Strong intensification of the Arabian Sea oxygen minimum zone in response to Arabian Gulf warming, *Geophys. Res. Lett.*, 46, 5420–5429, 2019.
- Lachkar, Z., Mehari, M., Al Azhar, M., Lévy, M., and Smith, S.: Fast local warming is the main driver of recent deoxygenation in the northern Arabian Sea, *Biogeosciences*, 18, 5831–5849, <https://doi.org/10.5194/bg-18-5831-2021>, 2021.
- Lachkar, Z., Lévy, M., Hailegeorgis, D., and Vallivatthillam, P.: Differences in recent and future trends in the Arabian Sea oxygen minimum zone: processes and uncertainties, *Frontiers in Marine Science*, 10, 1122043, <https://doi.org/10.3389/fmars.2023.1122043>, 2023.

- Levin, L. A.: Manifestation, drivers, and emergence of open ocean deoxygenation, *Annu. Rev. Mar. Sci.*, 10, 229–260, 2018.
- Lévy, M., Resplandy, L., Palter, J. B., Couespel, D., and Lachkar, Z.: The crucial contribution of mixing to present and future ocean oxygen distribution, in: *Ocean mixing*, edited by: Meredith, M. and Naviera Garabato, A., Elsevier, 329–344, <https://doi.org/10.1016/B978-0-12-821512-8.00020-7>, 2022.
- Liu, Q.-Y., Feng, M., Wang, D., and Wijffels, S.: Interannual variability of the Indonesian Throughflow transport: A revisit based on 30 year expendable bathythermograph data, *J. Geophys. Res.-Oceans*, 120, 8270–8282, 2015.
- Llanillo, P., Pelegrí, J. L., Talley, L., Peña-Izquierdo, J., and Cordero, R.: Oxygen pathways and budget for the eastern South Pacific oxygen minimum zone, *J. Geophys. Res.-Oceans*, 123, 1722–1744, 2018.
- Llewellyn, L. E., English, S., and Barnwell, S.: A roadmap to a sustainable Indian Ocean blue economy, *Journal of the Indian Ocean Region*, 12, 52–66, 2016.
- Luyten, J., Pedlosky, J., and Stommel, H.: The ventilated thermocline, *J. Phys. Oceanogr.*, 13, 292–309, 1983.
- Margolskee, A., Frenzel, H., Emerson, S., and Deutsch, C.: Ventilation pathways for the North Pacific oxygen deficient zone, *Global Biogeochem. Cy.*, 33, 875–890, 2019.
- McCarthy, M. C. and Talley, L. D.: Three-dimensional isoneutral potential vorticity structure in the Indian Ocean, *J. Geophys. Res.-Oceans*, 104, 13251–13267, 1999.
- McCarthy, M. C., Talley, L. D., and Baringer, M. O.: Deep upwelling and diffusivity in the southern Central Indian Basin, *Geophys. Res. Lett.*, 24, 2801–2804, 1997.
- McMonigal, K., Gunn, K. L., Beal, L. M., Elipot, S., and Willis, J. K.: Reduction in meridional heat export contributes to recent Indian Ocean warming, *J. Phys. Oceanogr.*, 52, 329–345, 2022.
- Menezes, V. V.: Advective pathways and transit times of the Red Sea Overflow Water in the Arabian Sea from Lagrangian simulations, *Prog. Oceanogr.*, 199, 102697, <https://doi.org/10.1016/j.pocean.2021.102697>, 2021.
- Miller, D., Poucher, S., and Coiro, L.: Determination of lethal dissolved oxygen levels for selected marine and estuarine fishes, crustaceans, and a bivalve, *Mar. Biol.*, 140, 287–296, 2002.
- Naqvi, S. W. A.: Deoxygenation in marginal seas of the Indian ocean, *Frontiers in Marine Science*, 8, 624322, <https://doi.org/10.3389/fmars.2021.624322>, 2021.
- O’Neill, B. C., Tebaldi, C., van Vuuren, D. P., Eyring, V., Friedlingstein, P., Hurtt, G., Knutti, R., Kriegler, E., Lamarque, J.-F., Lowe, J., Meehl, G. A., Moss, R., Riahi, K., and Sanderson, B. M.: The Scenario Model Intercomparison Project (ScenarioMIP) for CMIP6, *Geosci. Model Dev.*, 9, 3461–3482, <https://doi.org/10.5194/gmd-9-3461-2016>, 2016.
- Oschlies, A., Schulz, K. G., Riebesell, U., and Schmittner, A.: Simulated 21st century’s increase in oceanic suboxia by CO₂-enhanced biotic carbon export, *Global Biogeochem. Cy.*, 22, GB4008, <https://doi.org/10.1029/2007GB003147>, 2008.
- Oschlies, A., Brandt, P., Stramma, L., and Schmidtko, S.: Drivers and mechanisms of ocean deoxygenation, *Nat. Geosci.*, 11, 467–473, 2018.
- Paulmier, A. and Ruiz-Pino, D.: Oxygen minimum zones (OMZs) in the modern ocean, *Prog. Oceanogr.*, 80, 113–128, 2009.
- Pedlosky, J.: Eastern boundary ventilation and the structure of the thermocline, *J. Phys. Oceanogr.*, 13, 2038–2044, 1983.
- Phillips, H. E., Tandon, A., Furue, R., Hood, R., Ummerhofer, C. C., Benthuyesen, J. A., Menezes, V., Hu, S., Webber, B., Sanchez-Franks, A., Cherian, D., Shroyer, E., Feng, M., Wijesekera, H., Chatterjee, A., Yu, L., Hermes, J., Murtugudde, R., Tozuka, T., Su, D., Singh, A., Centurioni, L., Prakash, S., and Wiggert, J.: Progress in understanding of Indian Ocean circulation, variability, air–sea exchange, and impacts on biogeochemistry, *Ocean Sci.*, 17, 1677–1751, <https://doi.org/10.5194/os-17-1677-2021>, 2021.
- Piontkovski, S. and Al-Oufi, H.: The Omani shelf hypoxia and the warming Arabian Sea, *Int. J. Environ. Stud.*, 72, 256–264, 2015.
- Prince, E. D. and Goodyear, C. P.: Hypoxia-based habitat compression of tropical pelagic fishes, *Fish. Oceanogr.*, 15, 451–464, 2006.
- Queste, B. Y., Vic, C., Heywood, K. J., and Piontkovski, S. A.: Physical controls on oxygen distribution and denitrification potential in the north west Arabian Sea, *Geophys. Res. Lett.*, 45, 4143–4152, 2018.
- Rahmstorf, S., Box, J. E., Feulner, G., Mann, M. E., Robinson, A., Rutherford, S., and Schaffernicht, E. J.: Exceptional twentieth-century slowdown in Atlantic Ocean overturning circulation, *Nat. Clim. Change*, 5, 475–480, 2015.
- Resplandy, L.: Will ocean zones with low oxygen levels expand or shrink?, *Nature*, 557, 314–315, <https://doi.org/10.1038/d41586-018-05034-y>, 2018.
- Resplandy, L., Lévy, M., Bopp, L., Echevin, V., Pous, S., Sarma, V. V. S. S., and Kumar, D.: Controlling factors of the oxygen balance in the Arabian Sea’s OMZ, *Biogeosciences*, 9, 5095–5109, <https://doi.org/10.5194/bg-9-5095-2012>, 2012.
- Rhein, M., Stramma, L., and Plähn, O.: Tracer signals of the intermediate layer of the Arabian Sea, *Geophys. Res. Lett.*, 24, 2561–2564, 1997.
- Rixen, T., Cowie, G., Gaye, B., Goes, J., do Rosário Gomes, H., Hood, R. R., Lachkar, Z., Schmidt, H., Segsneider, J., and Singh, A.: Reviews and syntheses: Present, past, and future of the oxygen minimum zone in the northern Indian Ocean, *Biogeosciences*, 17, 6051–6080, <https://doi.org/10.5194/bg-17-6051-2020>, 2020.
- Roxy, M. K., Ritika, K., Terray, P., and Masson, S.: The curious case of Indian Ocean warming, *J. Climate*, 27, 8501–8509, 2014.
- Roy, A.: Blue economy in the Indian Ocean: Governance perspectives for sustainable development in the region, ORF Occasional Paper, 181, ISBN 978-93-88262-78-1, 2019.
- Schmidt, H., Getzlaff, J., Löptien, U., and Oschlies, A.: Causes of uncertainties in the representation of the Arabian Sea oxygen minimum zone in CMIP5 models, *Ocean Sci.*, 17, 1303–1320, <https://doi.org/10.5194/os-17-1303-2021>, 2021.
- Schmidtko, S., Stramma, L., and Visbeck, M.: Decline in global oceanic oxygen content during the past five decades, *Nature*, 542, 335–339, 2017.
- Schott, F. A., Dengler, M., and Schoenefeldt, R.: The shallow overturning circulation of the Indian Ocean, *Prog. Oceanogr.*, 53, 57–103, 2002.
- Schott, F. A., Xie, S.-P., and McCreary Jr., J. P.: Indian Ocean circulation and climate variability, *Rev. Geophys.*, 47, RG1002, <https://doi.org/10.1029/2007RG000245>, 2009.
- Schupfner, M., Wieners, K.-H., Wachsmann, F., Steger, C., Bittner, M., Jungclaus, J., Früh, B., Pankatz, K., Giorgetta, M., Reick, C., Legutke, S., Esch, M., Gayler, V., Haak, H., de Vrese, P., Rad-

- datz, T., Mauritsen, T., von Storch, J.-S., Behrens, J., Brovkin, V., Claussen, M., Crueger, T., Fast, I., Fiedler, S., Hagemann, S., Hohenegger, C., Jahns, T., Kloster, S., Kinne, S., Lasslop, G., Kornblueh, L., Marotzke, J., Matei, D., Meraner, K., Mikolajewicz, U., Modali, K., Müller, W., Nabel, J., Notz, D., Peters, K., Pincus, R., Pohlmann, H., Pongratz, J., Rast, S., Schmidt, H., Schnur, R., Schulzweida, U., Six, K., Stevens, B., Voigt, A., and Roeckner, E.: DKRZ MPI-ESM1.2-HR model output prepared for CMIP6 ScenarioMIP, World Climate Research Programme (WCRP) [data set], <https://doi.org/10.22033/ESGF/CMIP6.2450>, 2019.
- Seland, Ø., Bentsen, M., Olivieri, D., Toniazzo, T., Gjermundsen, A., Graff, L. S., Debernard, J. B., Gupta, A. K., He, Y.-C., Kirkevåg, A., Schwinger, J., Tjiputra, J., Aas, K. S., Bethke, I., Fan, Y., Griesfeller, J., Grini, A., Guo, C., Ilicak, M., Karset, I. H. H., Landgren, O., Liakka, J., Moseid, K. O., Nummelin, A., Spensberger, C., Tang, H., Zhang, Z., Heinze, C., Iversen, T., and Schulz, M.: Overview of the Norwegian Earth System Model (NorESM2) and key climate response of CMIP6 DECK, historical, and scenario simulations, *Geosci. Model Dev.*, 13, 6165–6200, <https://doi.org/10.5194/gmd-13-6165-2020>, 2020.
- Seland, Y., Bentsen, M., Olivieri, D. J. L., Toniazzo, T., Gjermundsen, A., Graff, L. S., Debernard, J. B., Gupta, A. K., He, Y., Kirkevåg, A., Schwinger, J., Tjiputra, J., Aas, K. S., Bethke, I., Fan, Y., Griesfeller, J., Grini, A., Guo, C., Ilicak, M., Karset, I. H. H., Landgren, O. A., Liakka, J., Moseid, K. O., Nummelin, A., Spensberger, C., Tang, H., Zhang, Z., Heinze, C., Iversen, T., and Schulz, M.: NCC NorESM2-LM model output prepared for CMIP6 CMIP, World Climate Research Programme (WCRP) [data set], <https://doi.org/10.22033/ESGF/CMIP6.502>, 2019a.
- Seland, Y., Bentsen, M., Olivieri, D. J. L., Toniazzo, T., Gjermundsen, A., Graff, L. S., Debernard, J. B., Gupta, A. K., He, Y., Kirkevåg, A., Schwinger, J., Tjiputra, J., Aas, K. S., Bethke, I., Fan, Y., Griesfeller, J., Grini, A., Guo, C., Ilicak, M., Karset, I. H. H., Landgren, O. A., Liakka, J., Moseid, K. O., Nummelin, A., Spensberger, C., Tang, H., Zhang, Z., Heinze, C., Iversen, T., and Schulz, M.: NCC NorESM2-LM model output prepared for CMIP6 ScenarioMIP, World Climate Research Programme (WCRP) [data set], <https://doi.org/10.22033/ESGF/CMIP6.604>, 2019b.
- Sen Gupta, A., McGregor, S., Van Sebille, E., Ganachaud, A., Brown, J. N., and Santoso, A.: Future changes to the Indonesian Throughflow and Pacific circulation: The differing role of wind and deep circulation changes, *Geophys. Res. Lett.*, 43, 1669–1678, 2016.
- Sharma, S., Ha, K.-J., Yamaguchi, R., Rodgers, K. B., Timmermann, A., and Chung, E.-S.: Future Indian Ocean warming patterns, *Nat. Commun.*, 14, 1789, 2023.
- Sheehan, P. M., Webber, B. G., Sanchez-Franks, A., Matthews, A. J., Heywood, K. J., and Vinayachandran, P.: Injection of oxygenated Persian Gulf Water into the southern Bay of Bengal, *Geophys. Res. Lett.*, 47, e2020GL087773, <https://doi.org/10.1029/2020GL087773>, 2020.
- Shrikumar, A., Lawrence, R., and Casciotti, K. L.: PYOMPA version 0.3, Authorea Preprints [code], <https://doi.org/10.1002/essoar.10507053.4>, 2022.
- Sprintall, J. and Tomczak, M.: On the formation of Central Water and thermocline ventilation in the southern hemisphere, *Deep-Sea Res. Pt. I*, 40, 827–848, 1993.
- Sprintall, J., Wijffels, S. E., Molcard, R., and Jaya, I.: Direct estimates of the Indonesian Throughflow entering the Indian Ocean: 2004–2006, *J. Geophys. Res.-Oceans*, 114, C07001, <https://doi.org/10.1029/2008JC005257>, 2009.
- Stellema, A., Sen Gupta, A., and Taschetto, A. S.: Projected slow down of South Indian Ocean circulation, *Sci. Rep.-UK*, 9, 1–15, 2019.
- Stramma, L., Johnson, G. C., Sprintall, J., and Mohrholz, V.: Expanding oxygen-minimum zones in the tropical oceans, *Science*, 320, 655–658, 2008.
- Stramma, L., Prince, E. D., Schmidtko, S., Luo, J., Hoolihan, J. P., Visbeck, M., Wallace, D. W., Brandt, P., and Körtzinger, A.: Expansion of oxygen minimum zones may reduce available habitat for tropical pelagic fishes, *Nat. Clim. Change*, 2, 33–37, 2012.
- Sun, S. and Thompson, A. F.: Centennial changes in the Indonesian Throughflow connected to the Atlantic meridional overturning circulation: The ocean's transient conveyor belt, *Geophys. Res. Lett.*, 47, e2020GL090615, <https://doi.org/10.1029/2020GL090615>, 2020.
- Tachiiri, K., Abe, M., Hajima, T., Arakawa, O., Suzuki, T., Komuro, Y., Ogochi, K., Watanabe, M., Yamamoto, A., Tatebe, H., Noguchi, M. A., Ohgaito, R., Ito, A., Yamazaki, D., Ito, A., Takata, K., Watanabe, S., and Kawamiya, M.: MIROC MIROC-ES2L model output prepared for CMIP6 ScenarioMIP, World Climate Research Programme (WCRP) [data set], <https://doi.org/10.22033/ESGF/CMIP6.936>, 2019.
- Takano, Y., Ito, T., and Deutsch, C.: Projected centennial oxygen trends and their attribution to distinct ocean climate forcings, *Global Biogeochem. Cy.*, 32, 1329–1349, 2018.
- Talley, L. D.: Descriptive physical oceanography: an introduction, Academic Press, ISBN 978-0-7506-4552-2, 2011.
- Tang, Y., Rumbold, S., Ellis, R., Kelley, D., Mulcahy, J., Selvar, A., Walton, J., and Jones, C.: MOHC UKESM1.0-LL model output prepared for CMIP6 CMIP, World Climate Research Programme (WCRP) [data set], <https://doi.org/10.22033/ESGF/CMIP6.1569>, 2019.
- Tomczak, M. and Large, D. G.: Optimum multiparameter analysis of mixing in the thermocline of the eastern Indian Ocean, *J. Geophys. Res.-Oceans*, 94, 16141–16149, 1989.
- Tomczak Jr., M.: A multi-parameter extension of temperature/salinity diagram techniques for the analysis of non-isopycnal mixing, *Prog. Oceanogr.*, 10, 147–171, 1981.
- Vallivattathillam, P., Lachkar, Z., and Lévy, M.: Shrinking of the Arabian Sea oxygen minimum zone with climate change projected with a downscaled model, *Frontiers in Marine Science*, 10, 1123739, <https://doi.org/10.3389/fmars.2023.1123739>, 2023.
- Vaquer-Sunyer, R. and Duarte, C. M.: Thresholds of hypoxia for marine biodiversity, *P. Natl. Acad. Sci. USA*, 105, 15452–15457, 2008.
- Wieners, K.-H., Giorgetta, M., Jungclaus, J., Reick, C., Esch, M., Bittner, M., Gayler, V., Haak, H., de Vrese, P., Raddatz, T., Mauritsen, T., von Storch, J.-S., Behrens, J., Brovkin, V., Claussen, M., Crueger, T., Fast, I., Fiedler, S., Hagemann, S., Hohenegger, C., Jahns, T., Kloster, S., Kinne, S., Lasslop, G., Kornblueh, L., Marotzke, J., Matei, D., Meraner, K., Mikolajewicz, U., Modali, K., Müller, W., Nabel, J., Notz, D., Peters, K., Pincus, R., Pohlmann, H., Pongratz, J., Rast, S., Schmidt, H., Schnur, R., Schulzweida, U., Six, K., Stevens, B., Voigt, A., and Roeckner, E.: MPI-M MPIESM1.2-LR model output prepared

- for CMIP6 ScenarioMIP, World Climate Research Programme (WCRP) [data set], <https://doi.org/10.22033/ESGF/CMIP6.793>, 2019a.
- Wieners, K.-H., Giorgetta, M., Jungclaus, J., Reick, C., Esch, M., Bittner, M., Legutke, S., Schupfner, M., Wachsmann, F., Gayler, V., Haak, H., de Vrese, P., Raddatz, T., Mauritsen, T., von Storch, J.-S., Behrens, J., Brovkin, V., Claussen, M., Crueger, T., Fast, I., Fiedler, S., Hagemann, S., Hohenegger, C., Jahns, T., Kloster, S., Kinne, S., Lasslop, G., Kornbluh, L., Marotzke, J., Matei, D., Meraner, K., Mikolajewicz, U., Modali, K., Müller, W., Nabel, J., Notz, D., Peters, K., Pincus, R., Pohlmann, H., Pongratz, J., Rast, S., Schmidt, H., Schnur, R., Schulzweida, U., Six, K., Stevens, B., Voigt, A., and Roeckner, E.: MPI-M MPIESM1.2-LR model output prepared for CMIP6 CMIP, World Climate Research Programme (WCRP) [data set], <https://doi.org/10.22033/ESGF/CMIP6.742>, 2019b.
- Zhuang, J., Dussin, R., Huard, D., Bourgault, P., Banihirwe, A., Hamman, J., Jüling, A., Filipe, Rondeau, G., Rasp, S., and Almansi, M.: pangeo-data/xESMF: v0.5.2, Zenodo [code], <https://doi.org/10.5281/zenodo.4464833>, 2021.